# Fabrication and Analysis of Gold Strip Plasmonic Waveguides Embedded in Chalcogenide

Damian Marek

Master of Engineering

Department of Electrical and Computer Engineering

McGill University 845 Sherbrooke St W Montreal, QC H3A 0G4 April. 15, 2014

A thesis submitted to McGill University in partial fulfillment of the requirements of the degree of Master of Engineering.

© Damian Marek 2014

### **Abstract**

This thesis aims to demonstrate surface plasmon polariton waveguides that can easily be end fire coupled to single mode fiber and provide high nonlinear phase shifts. Firstly, the theory of surface plasmons is developed and the existence of a propagating mode for a single and double interface structure is proven. Then the vector finite element method is introduced and used to reproduce results for a lossy dielectric waveguide. The ss0 mode of the finite width thin film waveguide is calculated and the convergence of the numerical method is shown. A waveguide with width 3 µm and thickness 10 nm is found to have the maximum nonlinear phase shift of 0.0012 rad·W<sup>-1</sup>. The fabrication process flow is explained as well as difficulties encountered. Finally, applications are discussed and suggestions are made for future work that could improve the performance of these waveguides.

## Résumé

Cette thèse rapporte l'étude du comportement de guides d'onde de plasmons de surface couplés avec des fibres optiques monomodes, et générant des déphasages non linéaire élevés. Premièrement, la théorie des plasmons de surface est examinée et l'existence d'un mode de surface pour des structures à interface simple et double est démontrée. Ensuite, la méthode vectorielle par éléments finis est introduite et utilisée afin de reproduire les résultats pour un guide d'onde diélectrique dissipatif. Le mode ss<sup>0</sup> d'un guide d'onde doté d'un mince film métallique de largeur finie est calculé et la convergence de la méthode numérique est présentée. De plus, il est démontré qu'un guide d'onde avec une largeur de 3 µm et une épaisseur de 10 nm présente un déphasage non linéaire maximal de 0.0012 rad·W-1. Le procédé de fabrication et les difficultés encourues à la réalisation expérimentale d'un prototype sont expliqués. Finalement, différentes applications sont mentionnées et de nouvelles méthodes d'analyse et de travail permettant d'accroître la performance des guides d'onde sont proposées.

# **Acknowledgments**

First, I would like to thank my supervisor Professor Martin Rochette for giving me free rein on choice of my research project. I am also grateful for his expertise in nonlinear photonics and willingness to help me to learn the concepts. I would also like to thank him for directly funding this project.

I am very grateful to Professor Juejun Hu from the University of Delaware and the rest of his group for performing many of the fabrication steps, most notably the deposition of Chalcogenide glass. He also provided an excellent knowledge base in microfabrication and addressed many of my questions.

I would also like to thank the staff and technicians at the McGill Nanotools Microfab for providing time, expertise and guidance in the fabrication process. Furthermore, the McGill Photonic Systems Group and its members provided excellent help in setting up the experiment.

Finally, I thank friends and family who patiently listened to me and provided feedback and reassurance.

# **Table of Contents**

Abstract		ii
Résumé		iii
Acknow	ledgments	iv
Table of	Figures	vii
Chapter	1: Introduction	9
Chapter	2: Plasmon Polariton Waves	12
2.1	Single Interface Plasmon Polaritons	13
2.1	1 TE Single Interface	14
2.1	2 TM Single Interface	15
2.2	Double Interface Surface Plasmon Polaritons	17
2.2	1 TE Double Interface	17
2.2	2 TM Double Interface	18
2.3	Modes of a Chalcogenide Gold Slab Plasmon Polariton Waveguide	19
2.4	Modes of a Symmetric Finite Width Thin Metal Film	22
Chapter	3: Third Order Nonlinearity of Waveguides	24
3.1	Nonlinear Index of Refraction	24
3.2	Self-Phase Modulation	25
3.3	Nonlinear Schrödinger Equation	27
Chapter	4: Simulation of Finite Width Thin Film Gold Strip Waveguides	29
4.1	The Vector Element Method	29
4.2	The Variational Method Formulation	31
4.3	Simulation of Chalcogenide Gold Strip Waveguides	37
4.4	Optimization of Chalcogenide Gold Strip Waveguide Design	42

4.5	Calculation of Coupling Coefficient Between SMF 28 and Plasmon	
Polari	ton Waveguide	. 43
Chapter	5: Fabrication and Experimentation of Gold Strip Waveguides	. 45
5.1	Fabrication Process	. 45
5.2	Loss Experimentation on Plasmon Polariton Waveguides	. 47
Chapter	6: Results and Conclusion	. 49
6.1	Results of Loss Experiment.	. 49
6.2	Conclusion	. 50
6.3	Future Work	. 52
Referen	ces	53

# **Table of Figures**

Figure 1: Schematic of a single a) and double b) interface structure. A propagat	ing
mode will propagate along z with constant β	. 13
Figure 2: Diagram of the two possible polarization configurations TE and TM.	
The propagation is in the z direction	. 13
Figure 3: Effective index of the two supported modes (asymmetric and	
symmetric), simulated using MatLab.	. 19
Figure 4: Loss of the two supported modes (asymmetric and symmetric),	
simulated using MatLab	. 20
Figure 5: Field components of symmetric mode for a 10 nm thick surface plasn	ıon
polariton waveguide. The focus is on the Ey component. Simulated with MatLa	.b
	. 21
Figure 6: Field components of symmetric mode for a 10 nm thick surface plasn	ıon
polariton waveguide. The focus is on the H <sub>x</sub> and E <sub>z</sub> components. Simulated wit	h
Matlab	. 21
Figure 7: The change in time domain and frequency domain of a Gaussian puls	e
with maximum phase shift, Phi, of 1.25 rad, 2.5 rad, 3.75 rad and 5 rad. Taken	
from [25]	. 28
Figure 8: The structure of a finite width thin gold strip waveguide.	. 29
Figure 9: A typical triangular element with edges and points labelled counter	
clockwise	. 30
Figure 10: The basis function corresponding to edge 1, with vector quantities	
represented by arrows.	. 31
Figure 11: Reproduction of loss results for MIS-CPW, simulated in MatLab	. 36
Figure 12: Reproduction of phase constant results for MIS-CPW, simulated in	
MatLab	. 37
Figure 13: Convergence of the phase constant as the number of elements is	
increased. Simulated in MatLab.	38

Figure 14: Mesh of simulation domain. Red represents the Chalcogenide glass,	
black represents the soda lime substrate and green represents the air. Simulated	,
using MatLab.	. 39
Figure 15: E <sub>y</sub> field of the lowest order ss mode of the gold film plasmon polarit	on
waveguide. Simulated using MatLab	. 40
Figure 16: E <sub>x</sub> field of the lowest order ss mode of the gold film plasmon polarit	on
waveguide. Simulated using MatLab.	. 41
Figure 17: E <sub>z</sub> field of the lowest order ss mode of the gold film plasmon polarit	on
waveguide. Simulated using MatLab.	. 41
Figure 18: Fabrication steps to construct gold strip plasmon polariton waveguid	les.
The diagrams are given from the transverse plane.	. 45
Figure 19: Facets after mechanical dicing. The dicing was a distance away from	1
the gold strips for a better result. A cleaved SMF is shown on the left	. 46
Figure 20: The dicing was moved closer to the waveguides and the results were	<b>;</b>
much worse. The two layers of Chalcogenide glass can be seen chipped away a	ıt
different positions. The gold layers are stripped much farther back from the edg	ge.
	. 47
Figure 21: Experimental setup of loss experiment.	. 47
Figure 22: The setup for coupling light in and out of the plasmon polariton	
waveguides (center). Translational stages were used on the two fiber clamps an	d
the microscope to have better control of the coupling	. 48
Figure 23: Loss measurement of plasmon polariton waveguide	49

# **Chapter 1: Introduction**

The motivation for current research into nonlinear photonics lies in the ability to extend the flexibility of photonics beyond the already broad possibilities of linear optics. The overall goal is to create original devices that can be made to complement electronics [1]. A subset of nonlinear photonics based on third order nonlinearities, which is described by  $n_2$  (m<sup>2</sup>/W), the nonlinear refractive index, has been used to create innovative devices such as frequency converters, frequency combs, modelocked lasers and supercontinuum generators [2]–[6]. Since the nonlinear response is usually quite low, nonlinear devices usually require large lengths and large field intensities.

Using plasmonics to induce high electric field intensities for enhancing nonlinear phenomena has been researched for the last two decades. The main method has been implanting metal particles or colloids into highly nonlinear dielectrics [1], [7]–[10]. The local field around the metal particles have high intensities for laser pulses with wavelengths close to the surface plasmon resonance of the individual particles [10]. This translates to an enhanced third order nonlinearity for the material. Another approach is based on the so-called long range surface plasmon polariton (LRSPP) [11]. The LRSPP is a propagating mode that exists for thin metal films encased in a dielectric. This mode is localized to the metal-dielectric interfaces and depending on the film thickness can be tailored to low loss or high field confinement [11]. Using a highly nonlinear dielectric as the cladding for such a waveguide can lead to an enhanced nonlinear response [12].

Another tool that researchers use to observe large nonlinear responses is to select dielectrics with high nonlinear refractive indices. One such group of materials extensively studied is the Chalcogenide glasses. These amorphous glass materials contain sulfur, selenium and/or tellurium as well as other elements like germanium or arsenic [13]. Many Chalcogenides have broad infrared transparency,

e.g.,  $Ge_{23}Sb_7S_{70}$  (1µm-10µm), and large nonlinear indices of refraction, e.g.,  $As_2Se_3$  (500 times larger than silica) [13], [14]. They also have large linear indices of refraction that facilitate the concentration of photons, e.g.,  $Ge_{23}Sb_7S_{70}$  (n = 2.15) and  $As_2Se_3$  (n = 2.83) [14], [15].

Maximizing the waveguide nonlinear coefficient,  $\gamma$ , while keeping losses low by designing different waveguide geometries with different materials has been studied extensively. Table 1 gives a few examples of these waveguide types and their nonlinear figure of merit (FOM). The figure of merit is a measure of a waveguide's nonlinear response, which includes loss. The nonlinear coefficient includes the effects of waveguide effective area and the material's nonlinear refractive index. This value multiplied by the effective length, which describes the loss, gives the waveguide's figure of merit.

*Table 1: Comparison of waveguide types and their Kerr nonlinear responses.* 

Waveguide type	Nonlinear index $n_2$ (m <sup>2</sup> /W)	Nonlinear coefficient γ (W <sup>-1</sup> ·m <sup>-1</sup> )	Loss α (dB/m)	Effective length L <sub>eff</sub> (m)	Nonlinear figure of merit (FOM) $\gamma \cdot L_{eff}(W^{-1})$
Highly nonlinear silica fiber [16]	2.2×10 <sup>-20</sup>	0.021	0.2	21715	91.20
Bismuth oxide fiber (Bi <sub>2</sub> O <sub>3</sub> ) [17],[18]	1.1×10 <sup>-18</sup>	1.36	0.8	5.42	7.38
As <sub>2</sub> S <sub>3</sub> waveguide [5]	3.0×10 <sup>-18</sup>	9.9	60	0.072	0.72
Silicon waveguide [19], [20]	4.5×10 <sup>-18</sup>	150	400	0.011	1.63
As <sub>2</sub> Se <sub>3</sub> microwires [14]	1.1×10 <sup>-17</sup>	187	<1	4.343	812.14

The objective of this thesis is to determine, through simulation and experimentation, if a large Kerr nonlinear response can be achieved by designing a gold strip surface plasmon waveguide with a suitable Chalcogenide glass as the cladding. The surface plasmon polariton's ability to strongly confine electric fields, should enhance the already high Kerr nonlinearity of Chalcogenide and result in a waveguide with a large nonlinear coefficient. However, the surface plasmon polaritons losses are expected to be high, so the waveguides' figure of merit,  $\gamma \cdot L_{eff}$ , will be calculated and compared to the results of Table 1.

This thesis is organized into six chapters. The second chapter, Plasmon Polariton Waves, introduces the theory for solving propagating modes of infinitely wide metal-dielectric waveguides with one or two metal-dielectric interfaces and briefly explains the notation for modes of a finite width thin film structure. The third chapter, Nonlinearity of Waveguides, presents the necessary background information on the third order Kerr nonlinearities present in optical waveguides and their effect on signal propagation. The fourth chapter, Simulation of Finite Width Thin Film Gold Strip Waveguides, explains the numerical simulation of the waveguides, the vector finite element method, and provides simulation results for different structures. The fifth chapter, Fabrication and Experimentation of Gold Strip Waveguides, describes the fabrication process of the waveguides and the experimental setup for the loss characterization. The sixth and final chapter, Results and Conclusion, discusses the results and provides feedback for future research in this area.

# **Chapter 2: Plasmon Polariton Waves**

A surface plasmon polariton is defined as a surface oscillation of electrons coupled with a photon at the interface between a material that has a positive permittivity, usually a dielectric, and a material that has a negative permittivity, usually a metal [21]. There are other cases where surface plasmons may exist, such as interfaces that include materials with non-unity magnetic permeability. This thesis will consider only the case of an interface bounded by a dielectric and a metal with a relative magnetic permeability of 1, or non-magnetic media [21].

Two geometries will be considered: a single interface between dielectric and metal and a double interface between dielectric and metals. Figure 1 shows the structure of a single interface and double interface structure.

These two-dimensional structures offer no confinement along the *x* axis and therefore have little practical interest, especially for nonlinear processes. However, the solutions offer a good approximation for the thin film finite width structure considered later in Chapter 4.

The modes of these structures are rigorously derived so that the reader may better understand the modes of a finite width thin film structure studied in Chapter 4. The  $ss^0$  mode of the finite width thin film waveguide shares many characteristics with the symmetric mode of the double interface structure. The most important is the reliance of the loss and field confinement on the metal thickness. The single interface structure is solved because the modes of a double interface can be thought of as two single interface modes that are coupled together. Furthermore, the derivation is fairly simple and demonstrates the interesting ability of surface plasmons to be bound to a single interface unlike modes of a dielectric waveguide. Finally, the TM (Transverse Magnetic) nature of these slab guide modes is an important effect and is shared by the  $ss^0$  mode of the finite width thin film waveguide.

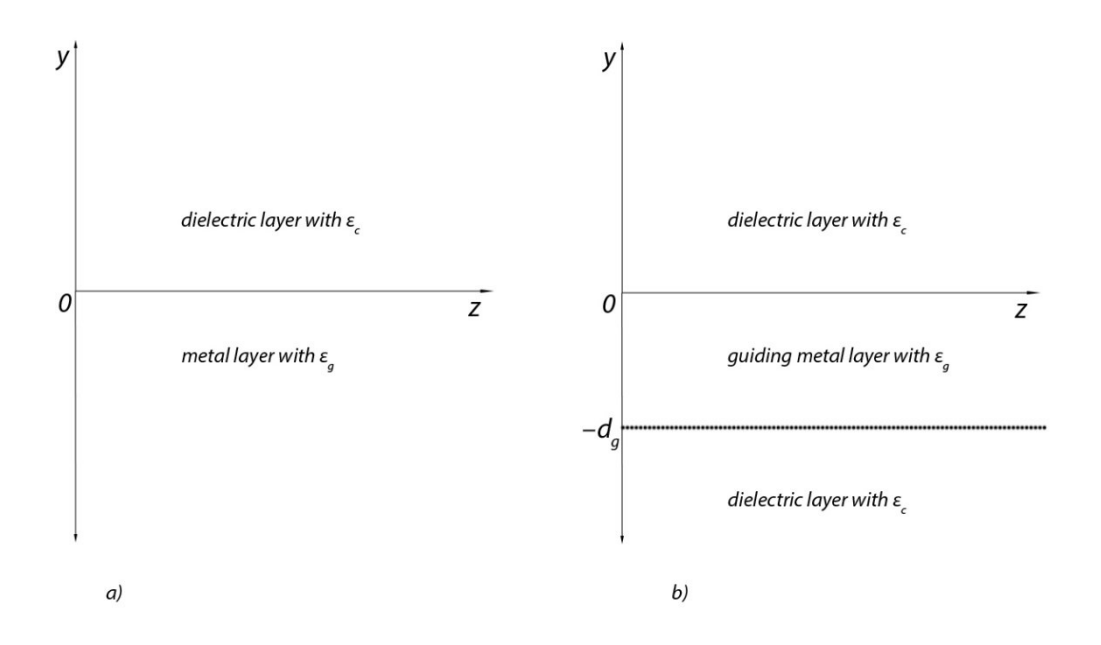


Figure 1: Schematic of a single a) and double b) interface structure. A propagating mode will propagate along z with constant  $\beta$ .

#### 2.1 Single Interface Plasmon Polaritons

First a field description and mode solution will be developed for the single interface geometry for two polarizations: TE (Transverse Electric) and TM (Transverse Magnetic). Both polarizations have only three field components.

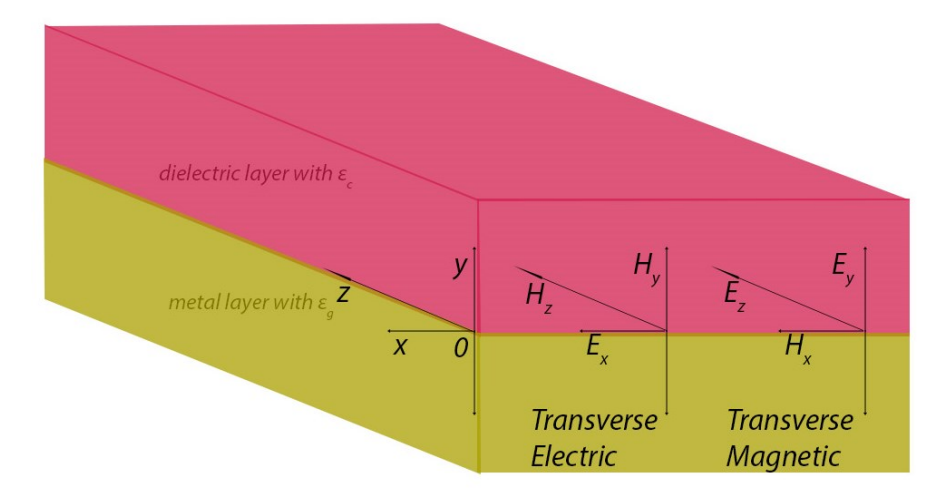


Figure 2: Diagram of the two possible polarization configurations TE and TM. The propagation is in the z direction.

The TE mode has only a single electric field component along the *x* axis. The TM mode has only a single magnetic field component along the *x* axis as shown in Figure 2.

It will be demonstrated that only one of these polarizations is able to excite a propagating mode. The electromagnetic fields are represented by monochromatic waves as in equations (2.1) and (2.2).

$$\mathbf{E}(\mathbf{r},t) = Re\{\mathbf{E}(\mathbf{r})e^{j\omega t}\}\tag{2.1}$$

$$H(r,t) = Re\{H(r)e^{j\omega t}\}$$
(2.2)

The wave vectors are given by the following equations, where  $k_0 = 2\pi/\lambda$  and  $\delta$ ,  $\gamma$  are the transverse normalized wavenumbers [21].

$$\beta = \frac{k_z}{k_0} \tag{2.3}$$

$$\delta^2 = \beta^2 - \varepsilon_c \mu_c \tag{2.4}$$

$$\gamma^2 = \beta^2 - \varepsilon_g \mu_g \tag{2.5}$$

#### 2.1.1 TE Single Interface

For a TE mode, there is one electric field component  $E_x$  and two magnetic fields  $H_y$  and  $H_z$ . For a planar propagating wave, the  $E_x$  is given by equation (2.6) [21].

$$E_{x} = E_{0}e^{-j(k_{y}y + k_{0}\beta z)} \tag{2.6}$$

In this case,  $k_y = -jk_0\delta$  or  $jk_0\gamma$  depending on which material the field lies in. The fields must be evanescent along y for a propagating mode that forces  $k_y$  to these values, assuming real positive values for  $\delta$  and  $\gamma$ . This can be directly expressed by equation (2.7).

$$E_{x} = E_{0}e^{-jk_{0}\beta z} \begin{pmatrix} e^{-k_{0}\delta y} & y > 0 \\ e^{k_{0}\gamma y} & y < 0 \end{pmatrix}$$

$$(2.7)$$

From Maxwell's equations and the wave equation, the magnetic field can be written in terms of the electric field by equation (2.8).

$$H_{y} = \frac{j}{\mu_{0}\mu_{r}\omega} \frac{\partial}{\partial z} E_{x} \tag{2.8}$$

Putting equation (2.14) into equation (2.8) results in an explicit form of the magnetic field

$$H_{y} = E_{0} \frac{k_{0} \beta}{\mu_{0} \omega} e^{-jk_{0} \beta z} \begin{pmatrix} \frac{1}{\mu_{c}} e^{-k_{0} \delta y} & y > 0\\ \frac{1}{\mu_{d}} e^{k_{0} \gamma y} & y < 0 \end{pmatrix}.$$
 (2.9)

This same process can be repeated for the  $H_z$  component as shown by equation (2.10) and (2.11).

$$H_z = \frac{-j}{\mu_0 \mu_r \omega} \frac{\partial}{\partial y} E_x \tag{2.10}$$

$$H_z = E_0 \frac{jk_0}{\mu_0 \omega} e^{-jk_0 \beta z} \begin{pmatrix} \frac{\delta}{\mu_c} e^{-k_0 \delta y} & y > 0\\ \frac{-\gamma}{\mu_a} e^{k_0 \gamma y} & y < 0 \end{pmatrix}$$
(2.11)

The boundary conditions dictate that the tangential components of the electric and magnetic fields must be continuous [21]. Continuity of  $H_z$  leads to the dispersion equation (2.12).

$$\frac{\delta}{\mu_c} = -\frac{\gamma}{\mu_g} \tag{2.12}$$

Since the original assumption was that  $\delta$  and  $\gamma$  are real and positive, the values for magnetic permeability must have opposite signs. These kinds of materials are possible but for our case of dielectric and metal that are non-magnetic, it is not. Thus, at such an interface there will not be a supported mode for TE fields.

#### 2.1.2 TM Single Interface

The exact same approach can be taken for a TM mode for which there are  $H_x$ ,  $E_y$  and  $E_z$  fields. The results are shown for the 3 fields in (2.13), (2.14) and (2.15).

$$H_{x} = H_{0}e^{-jk_{0}\beta z} \begin{pmatrix} e^{-k_{0}\delta y} & y > 0 \\ e^{k_{0}\gamma y} & y < 0 \end{pmatrix}$$
 (2.13)

$$E_{y} = -H_{0} \frac{k_{0}\beta}{\varepsilon_{0}\omega} e^{-jk_{0}\beta z} \begin{pmatrix} \frac{1}{\varepsilon_{c}} e^{-k_{0}\delta y} & y > 0\\ \frac{1}{\varepsilon_{a}} e^{k_{0}\gamma y} & y < 0 \end{pmatrix}$$
(2.14)

$$E_{z} = H_{0} \frac{jk_{0}}{\varepsilon_{0}\omega} e^{-jk_{0}\beta z} \begin{pmatrix} -\frac{\delta}{\varepsilon_{c}} e^{-k_{0}\delta y} & y > 0\\ \frac{\gamma}{\varepsilon_{q}} e^{k_{0}\gamma y} & y < 0 \end{pmatrix}$$
(2.15)

The boundary conditions are the same, but now the condition is

$$\frac{\delta}{\varepsilon_c} = -\frac{\gamma}{\varepsilon_g} \ . \tag{2.16}$$

Similar to the TE case, the relative permittivities must have opposite signs. This will be possible since metals have a negative permittivity. Replacing (2.16) with expressions in terms of  $\beta$  yields

$$\frac{\beta^2 - \varepsilon_c \mu_c}{\varepsilon_c^2} = \frac{\beta^2 - \varepsilon_g \mu_g}{\varepsilon_g^2} \,. \tag{2.17}$$

Solving for  $\beta$  in (2.17) gives the solution for the propagation constant

$$\beta = \sqrt{\frac{\mu_c \varepsilon_c \varepsilon_g^2 - \mu_g \varepsilon_g \varepsilon_c^2}{\varepsilon_g^2 - \varepsilon_c^2}}.$$
 (2.18)

For non-magnetic medium  $\mu_g = \mu_c = 1$ , the solution simplifies to

$$\beta = \sqrt{\frac{\varepsilon_c \varepsilon_g}{\varepsilon_g + \varepsilon_c}}.$$
 (2.19)

This means that there exists a bound propagating mode for a single interface structure, which is not possible to achieve with a similar dielectric structure. Physically this is possible because the photons are coupling with plasmons or coherent groups of oscillating electrons [21]. The fields of this mode are TM and only have a single transverse electric field perpendicular to the interface. The field profile is exponential on both sides of the interface, but the electric and magnetic fields penetrate much farther into the dielectric. Since there is still a significant portion of the field inside the metal, the propagation losses are quite high. Propagation lengths are generally in the  $\mu$ m range. The wavenumber will be much larger than that of a photon with the same frequency travelling in a dielectric, so coupling light to a surface plasmon polariton is not easy with end fire techniques.

The next section, Double Interface Surface Plasmon Polaritons, will explain how the propagation length can be orders of magnitude longer for thin metal films sandwiched between dielectrics. The symmetric mode of a double interface structure has the added benefit of a smaller wavenumber value and coupling by end firing can be much easier.

#### 2.2 Double Interface Surface Plasmon Polaritons

#### 2.2.1 TE Double Interface

For the double interface case, a guiding layer of relative permittivity  $\varepsilon_g$  is surrounded by a dielectric of  $\varepsilon_c$ . Assuming evanescent decay in the cladding for a propagating mode (2.28) gives the field description. Also by introducing a new component of the wave vector propagating in the guiding layer, given by (2.31), the complete description can be given by,

$$\kappa^2 = \varepsilon_a \mu_a - \beta^2 \,, \tag{2.20}$$

where  $\kappa$  is dominantly real and positive in a low loss medium. In a metal with negative  $\varepsilon_g$ ,  $\kappa$  will be mainly imaginary, which suggests that hyperbolic basis functions would also be suitable for the core [22].

$$E_{x} = e^{-jk_{0}\beta z} \begin{pmatrix} Ae^{-k_{0}\delta y} & y \ge 0 \\ A\cos(k_{0}\kappa y) + B\sin(k_{0}\kappa y) & -d_{g} < y < 0 \\ (A\cos(k_{0}\kappa d_{g}) - B\sin(k_{0}\kappa d_{g}))e^{k_{0}\delta(d_{g}+y)} & y \le -d_{g} \end{pmatrix}$$

$$(2.21)$$

Using (2.8) the  $H_y$  field distribution can be written

$$H_{y} = \frac{k_{0}\beta}{\mu_{0}\omega} e^{-jk_{0}\beta z} \begin{pmatrix} \frac{1}{\mu_{c}} A e^{-k_{0}\delta y} & y \geq 0\\ \frac{1}{\mu_{g}} (A\cos(k_{0}\kappa y) + B\sin(k_{0}\kappa y)) & -d_{g} < y < 0\\ \frac{1}{\mu_{c}} (A\cos(k_{0}\kappa d_{g}) - B\sin(k_{0}\kappa d_{g})) e^{k_{0}\delta(d_{g} + y)} y \leq -d_{g} \end{pmatrix}.$$
 (2.22)

Using (2.10) the  $H_z$  field distribution can be written

$$H_{Z} = \frac{-jk_{0}}{\mu_{0}\omega} e^{-jk_{0}\beta z} \begin{pmatrix} -\frac{\delta}{\mu_{c}} A e^{-k_{0}\delta y} & y \geq 0\\ \frac{\kappa}{\mu_{g}} (-A\sin(k_{0}\kappa y) + B\cos(k_{0}\kappa y)) & -d_{g} < y < 0\\ \frac{\delta}{\mu_{c}} (A\cos(k_{0}\kappa d_{g}) - B\sin(k_{0}\kappa d_{g})) e^{k_{0}\delta(d_{g}+y)} & y \leq -d_{g} \end{pmatrix}. \tag{2.23}$$

The boundary conditions dictate that the tangential magnetic and electric fields are equal at the interfaces. For the  $H_z$  field at y = 0, an expression for A and B can be found.

$$-\frac{\delta}{\mu_c} \frac{\mu_g}{\kappa} A = B \tag{2.24}$$

Using this expression for B, the boundary condition at  $y = -d_g$  can be written.

$$\frac{\kappa}{\mu_g}(\sin(k_0\kappa d_g) - \frac{\delta}{\mu_c}\frac{\mu_g}{\kappa}\cos(k_0\kappa d_g)) = \frac{\delta}{\mu_c}(\cos(k_0\kappa d_g) + \frac{\delta}{\mu_c}\frac{\mu_g}{\kappa}\sin(k_0\kappa d_g))$$
(2.25)

Rearranging the terms and assuming  $\mu_s = \mu_c = 1$ , the solution simplifies to

$$tan(k_0 \kappa d_g) = \kappa \frac{2\delta}{\kappa^2 - \delta^2}.$$
 (2.26)

It is not easily seen from this formula, but if the two materials have opposite signs for the electric permittivity, then there is no solution to this equation. Thus, similar to the single interface case, no TE mode exists.

#### 2.2.2 TM Double Interface

With only a few changes, all the previous algebra can be repeated to find the three field distributions for a TM mode.

$$H_{x} = e^{-jk_{0}\beta z} \begin{pmatrix} Ae^{-k_{0}\delta y} & y \geq 0 \\ A\cos(k_{0}\kappa y) + B\sin(k_{0}\kappa y) & -d_{g} < y < 0 \\ (A\cos(k_{0}\kappa d_{g}) - B\sin(k_{0}\kappa d_{g}))e^{k_{0}\delta(d_{g}+y)} & y \leq -d_{g} \end{pmatrix}$$

$$(2.27)$$

$$H_{x} = e^{-jk_{0}\beta z} \begin{pmatrix} Ae^{-k_{0}\delta y} & y \geq 0 \\ A\cos(k_{0}\kappa y) + B\sin(k_{0}\kappa y) & -d_{g} < y < 0 \\ (A\cos(k_{0}\kappa d_{g}) - B\sin(k_{0}\kappa d_{g}))e^{k_{0}\delta(d_{g}+y)} & y \leq -d_{g} \end{pmatrix}$$

$$E_{y} = \frac{-k_{0}\beta}{\varepsilon_{0}\omega} e^{-jk_{0}\beta z} \begin{pmatrix} \frac{1}{\varepsilon_{c}}Ae^{-k_{0}\delta y} & y \geq 0 \\ \frac{1}{\varepsilon_{g}}(A\cos(k_{0}\kappa y) + B\sin(k_{0}\kappa y)) & -d_{g} < y < 0 \\ \frac{1}{\varepsilon_{c}}(A\cos(k_{0}\kappa d_{g}) - B\sin(k_{0}\kappa d_{g}))e^{k_{0}\delta(d_{g}+y)} & y \leq -d_{g} \end{pmatrix}$$

$$E_{z} = \frac{jk_{0}}{\varepsilon_{0}\omega} e^{-jk_{0}\beta z} \begin{pmatrix} -\frac{\delta}{\varepsilon_{c}}Ae^{-k_{0}\delta y} & y \geq 0 \\ \frac{\kappa}{\varepsilon_{g}}(-A\sin(k_{0}\kappa y) + B\cos(k_{0}\kappa y)) & -d_{g} < y < 0 \\ \frac{\delta}{\varepsilon_{c}}(A\cos(k_{0}\kappa d_{g}) - B\sin(k_{0}\kappa d_{g}))e^{k_{0}\delta(d_{g}+y)} & y \leq -d_{g} \end{pmatrix}$$

$$(2.27)$$

$$E_{z} = \frac{jk_{0}}{\varepsilon_{0}\omega}e^{-jk_{0}\beta z} \begin{pmatrix} -\frac{\delta}{\varepsilon_{c}}Ae^{-k_{0}\delta y} & y \geq 0\\ \frac{\kappa}{\varepsilon_{g}}(-A\sin(k_{0}\kappa y) + B\cos(k_{0}\kappa y)) & -d_{g} < y < 0\\ \frac{\delta}{\varepsilon_{c}}(A\cos(k_{0}\kappa d_{g}) - B\sin(k_{0}\kappa d_{g}))e^{k_{0}\delta(d_{g}+y)} & y \leq -d_{g} \end{pmatrix}$$

$$(2.29)$$

Again using the same approach as for the TE case, solving both boundary conditions gives dispersion relation

$$tan(k_0 \kappa d_g) = \frac{2\varepsilon_c \varepsilon_g \delta \kappa}{\varepsilon_c^2 \kappa^2 - \varepsilon_g^2 \delta^2}.$$
 (2.30)

(2.30) can be further reduced to give even and odd solutions

$$tan(k_0 \kappa d_g/2) = \frac{\varepsilon_g \delta}{\varepsilon_c \kappa}, \qquad (2.31)$$

$$tan(k_0\kappa d_g/2) = -\frac{\varepsilon_c \kappa}{\varepsilon_g \delta}, \qquad (2.32)$$

where (2.31) is the even mode and (2.32) is the solution to the odd mode [21]. Similar to the single interface geometry, all the fields are evanescently decaying. The metal guiding layer is also exponential decaying since the transverse component of the wave vector is predominantly imaginary. For very thin films, the effective index evolves into that of a plane wave propagating in the surround dielectric. This property makes the symmetric mode a good candidate for end fire coupling.

#### 2.3 Modes of a Chalcogenide Gold Slab Plasmon Polariton Waveguide

Using Figure 1 as a reference, consider a symmetric structure composed of  $Ge_{23}Sb_7S_{70}$  as the dielectric layers and a thin gold film for the core layer. These materials, at an illumination wavelength of 1550 nm, have permittivities of  $\varepsilon_c$  = 4.84 and  $\varepsilon_g$  = -131.95 – 12.65j [15], [23]. With these values the dispersion equation (2.30) can be solved as a function of thickness, as shown in Figure 3 and Figure 4.

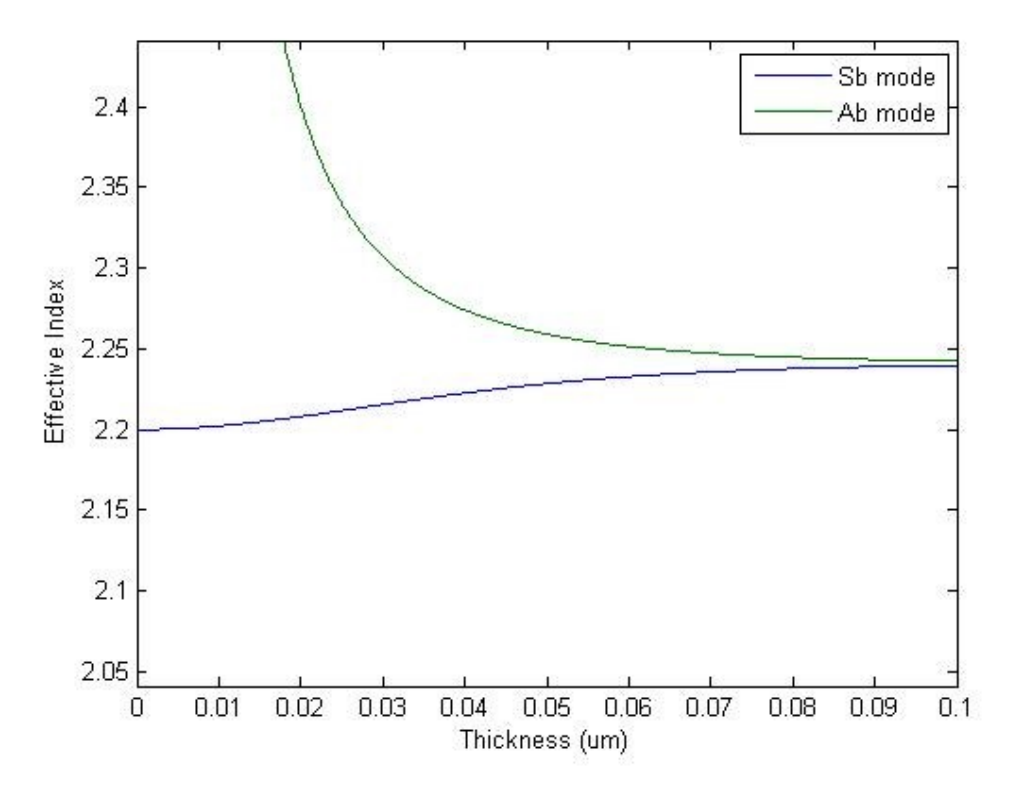


Figure 3: Effective index of the two supported modes (asymmetric and symmetric), simulated using MatLab.

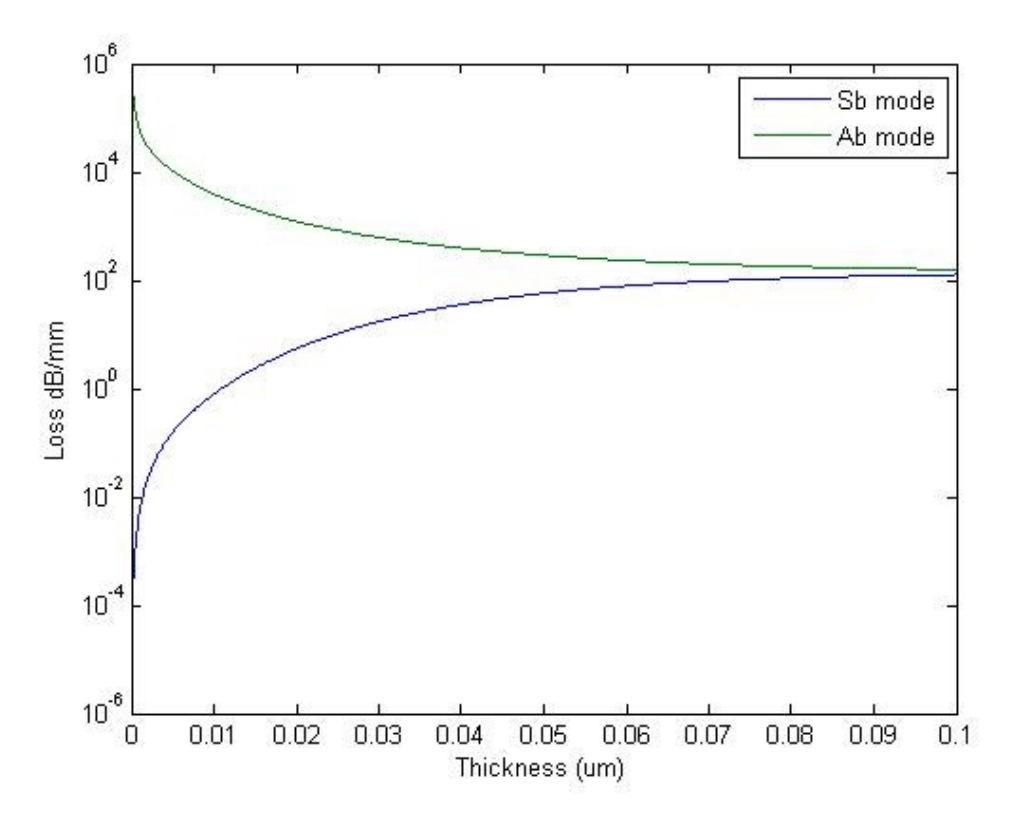


Figure 4: Loss of the two supported modes (asymmetric and symmetric), simulated using MatLab.

These are the well-known symmetric and asymmetric modes, and refer to the symmetry of the dominant field component, in this case Ey [11]. They are also called the long range surface plasmon polariton (LRSPP) and the short range surface plasmon polariton (SRSPP) because of their attenuation characteristics [11]. The LRSPP attenuation decreases to zero for small thicknesses and the opposite is true for the SRSPP. For both modes, as the thickness increases the modes become degenerate and evolve into the single interface solution [11]. These solutions provide a good approximation of the two main types of bound modes that exist for a thin metal film of finite width [11]. The field distribution of the symmetric mode is useful to analyse as it is similar to the mode of interest for the finite width case. For a very thin waveguide, the symmetric mode extends deep into the dielectric and thus experiences less loss. An example is given by

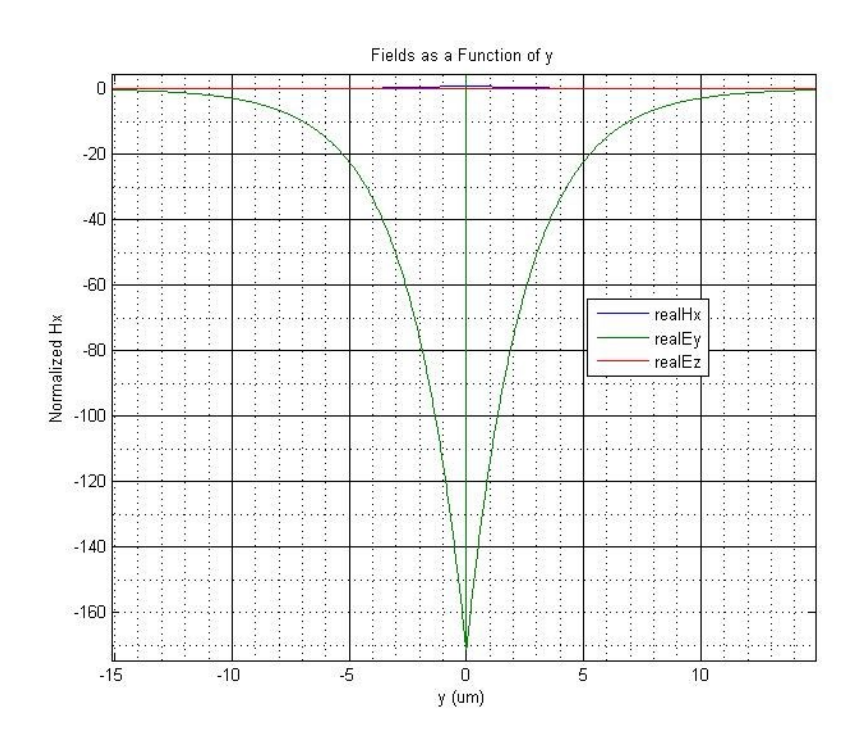


Figure 5: Field components of symmetric mode for a 10 nm thick surface plasmon polariton waveguide. The focus is on the  $E_y$  component. Simulated with MatLab

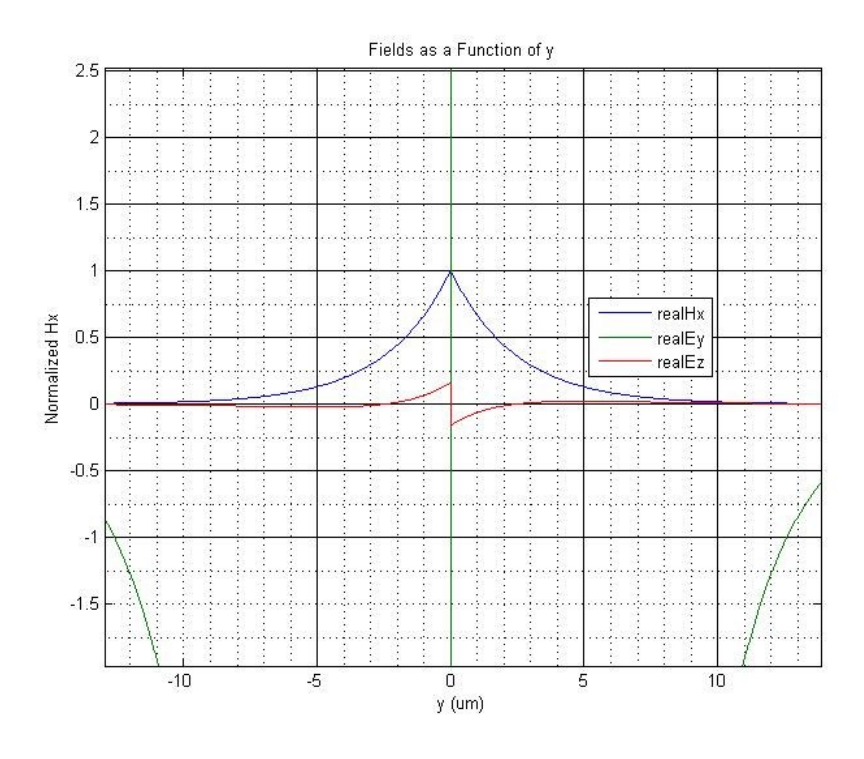


Figure 6: Field components of symmetric mode for a 10 nm thick surface plasmon polariton waveguide. The focus is on the  $H_x$  and  $E_z$  components. Simulated with Matlab

Figure 5 and Figure 6, which describe the symmetric mode of a 10 nm thick Chalcogenide and gold structure. For the symmetric mode, as the thickness becomes smaller the transverse electric field becomes larger when compared to the remaining two. On the other hand, the asymmetric mode penetrates farther into the metal for small thicknesses and has larger losses. As a consequence the electric field is confined tightly to the metal-dielectric interface.

#### 2.4 Modes of a Symmetric Finite Width Thin Metal Film

Now that the symmetric and asymmetric modes of the slab type waveguides have been characterized, it is useful to classify the modes that exist for a finite width structure. It will be seen that the  $ss^0$  mode has characteristics that make it useful for coupling to optical fibers and propagating longer distances.

As will be shown in Chapter 4, the *ss* modes share the important characteristic of having lower losses for thinner waveguides [11]. In many ways the *ss* mode of a finite width waveguide is very similar to the symmetric mode of a slab type waveguide. The phase constant approaches the value for a plane wave propagating in the surrounding dielectric, which makes end fire coupling possible. This is a useful guess that can be used to initialize the finite element method used in Chapter 4. This numbering maxima scheme was developed with thicker metal films in mind.

In a very thin film, the  $ss^0$  mode field profile encompasses the entire metal structure and so it does have a maximum along the horizontal and vertical directions.

# **Chapter 3: Third Order Nonlinearity of**

# Waveguides

Simply put, a nonlinear medium is a material where the polarization density and electric field relation (3.21) is not linear [24], [25].

$$\mathbf{P} = \varepsilon_0 \chi \mathbf{E} \tag{3.1}$$

The tensor notation for  $\chi$  (the electric susceptibility) is dropped and the medium is assumed to be isotropic. In fact most materials will have a nonlinear response when the applied electrical field is proportional to the interatomic electric fields and can be described by equation (3.2) [24].

$$\mathbf{P} = \varepsilon_0 \chi_1 \mathbf{E} + \varepsilon_0 \chi_2 \mathbf{E} \mathbf{E} + \varepsilon_0 \chi_3 \mathbf{E} \mathbf{E} \mathbf{E} + \cdots$$
 (3.2)

#### 3.1 Nonlinear Index of Refraction

The nonlinear electric susceptibility is a property of the material and in the case of Chalcogenide has a very low second order response. The higher order susceptibilities can be ignored and equation (3.2) can be simplified.

$$\mathbf{P} = \varepsilon_0 \chi_1 \mathbf{E} + \varepsilon_0 \chi_3 \mathbf{E} \mathbf{E} \mathbf{E} \tag{3.3}$$

Focusing on the nonlinear half of equation (3.3) and substituting the expression for a harmonic field results in,

$$\mathbf{P}_{NL} = \varepsilon_0 \chi_3 \left( \frac{3E_0^2 E_0^*}{8} e^{j\omega t} + \frac{E_0^3}{8} e^{j3\omega t} + c.c. \right), \tag{3.4}$$

where  $E_{\theta}$  is a complex amplitude and c.c. stands for the complex conjugate. The mechanism for third harmonic generation can be seen from this equation and is a direct result of third order nonlinearity. The other component is responsible for the Kerr effect. If the third harmonic generation is ignored for now and equation (3.4) is reordered, an expression for the Kerr effect can be realized [16].

$$\mathbf{P} = \varepsilon_0 \chi_1 \mathbf{E} + \frac{3|E_0|^2}{4} \varepsilon_0 \chi_3 \mathbf{E}$$
 (3.5)

Then using the relation between electric permittivity and index of refraction, the nonlinear index of refraction and absorption coefficient can be expressed by equation (3.6) and (3.7) [16].

$$n = n_0 + n_2 |E_0|^2 (3.6)$$

$$\alpha = \alpha_0 + \alpha_2 |E_0|^2 \tag{3.7}$$

Remembering to use the sign convention for harmonic waves expressed in equation (2.1), the nonlinear components of the index of refraction and absorption coefficient can be related to the electric susceptibility by equations (3.8) and (3.9) [16].

$$n_2 = \frac{3}{8n_0} Re\{\chi_3\} \tag{3.8}$$

$$\alpha_2 = -\frac{3}{4}k_0 Im\{\chi_3\} \tag{3.9}$$

The effect of the index of refraction depending on the incident intensity of light is the mechanism for self-phase modulation and cross-phase modulation.

#### 3.2 Self-Phase Modulation

The phase of a travelling wave is given by [16]

$$\varphi = \omega t - \beta z + \varphi_{0} \tag{3.10}$$

where  $\beta$  is the propagation constant. Replacing its value in a nonlinear medium gives the intensity dependent phase shift [16].

$$\varphi = \omega t - k_0 (n_0 + n_2 |E_0|^2) z + \varphi_0$$
(3.11)

This phase shift causes a chirp and change in instantaneous frequency, which can be described by equation (3.12) [16].

$$\omega_i = \omega - k_0 n_2 \frac{d|E_0|^2}{dt} z \tag{3.12}$$

A useful metric for describing the amount of phase shift accumulated over propagation distance is the maximum phase shift given by equation (3.13) [16].

$$\Delta \varphi_{max} = k_0 (n_2 |E_0|^2) L \tag{3.13}$$

For an optical pulse, the middle or peak of the pulse experiences the maximum phase shift. If the expression in (3.13) is changed to incorporate intensity, then the maximum phase shift can be described by the peak pulse power.

$$\Delta \varphi_{max} = \frac{k_0 (n_2^I P_{Max}) L}{A_{eff}}$$
 (3.14)

The two new variables  $n_2^I$  and  $A_{eff}$  are the nonlinear refractive index in power units and the effective mode area [16].

$$n_2^I = \frac{n_2}{2cn_0\varepsilon_0} {3.15}$$

$$A_{eff} = \frac{(\iint |F(x,y)|^2 dx dy)^2}{\iint (|F(x,y)|^4 dx dy)}$$
(3.16)

F(x, y) is the mode distribution. From these parameters, it is evident that decreasing the effective mode area and increasing the peak pulse power will increase the maximum phase shift. It is also possible to accumulate a larger phase shift by propagating over long distances. Another variable usually defined as  $\gamma$  is the nonlinear parameter, which is useful for characterizing waveguides [16].

$$\gamma = \frac{k_0 n_2^I}{A_{eff}} \tag{3.17}$$

The nonlinear length,  $L_{NL}$ , is an indication over what distances the phase shift has a noticeable impact on optical pulses [16].

$$L_{NL} = \frac{1}{\gamma P_{Max}} \tag{3.18}$$

More precisely  $L_{NL}$  is the length at which the maximum phase shift is 1 radian. In lossy waveguides, attenuation plays an important role and must be considered. The equivalent propagation length through a lossless waveguide is used and replaces L [16].

$$L_{eff} = \frac{1 - e^{-\alpha L}}{\alpha} \tag{3.19}$$

Now the maximum phase shift can be stated in term of the effective length and the nonlinear length.

$$\Delta \varphi_{max} = \frac{L_{eff}}{L_{NL}} \tag{3.20}$$

When losses are involved, a waveguide's nonlinear response is usually described by the figure of merit (FOM),  $\gamma \cdot L_{\text{eff}}$ . The effective length is then calculated with the

length of the waveguide set to infinity. The figure of merit is then given by equation (3.21) [14].

$$FOM = \frac{k_0 n_2^I}{A_{eff} \alpha} \tag{3.21}$$

#### 3.3 Nonlinear Schrödinger Equation

Since the Kerr effect is dependent on field intensity, it is important to determine its effect on optical pulses. The differential equation that describes the change in mode propagation is derived from first-order perturbation theory [16]. If the overall shape of the time pulse is given as A and is assumed to vary with z, the effect of dispersion, attenuation and the Kerr effect is given by the nonlinear Schrödinger equation (NLSE) [16].

$$\frac{\partial A}{\partial z} - j \frac{\beta_2}{2} \frac{\partial^2 A}{\partial T^2} + \frac{\alpha}{2} A + j \gamma |A|^2 A = 0$$
 (3.22)

In the NLSE,  $\beta_2$  is related to chromatic dispersion and T is the time in a reference frame travelling with the pulse [16]. The difference of sign between equation (3.22) and the reference [16] comes from the different sign convention of time harmonic fields.

The NLSE can be solved numerically by using the Split-step Fourier method. Since dispersion is easier to address in the frequency domain and the Kerr effect in the time domain, the propagation length is discretized. In each small discretization, the dispersion and Kerr effect are applied independently to the input signal, first by applying the dispersion in the frequency domain and then after an inverse Fourier transform, applying the Kerr effect [16].

The evolution of a Gaussian pulse with peak power 1 mW and waveguide nonlinear parameter 0.1 m<sup>-1</sup>W<sup>-1</sup> is shown in Figure 7. Assuming the only effect is due to Kerr nonlinearity, the self-phase modulation causes the frequency spectrum to widen and form peaks. As the pulse accumulates larger phase shifts, the spectrum continually forms new peaks. However, the induced phase has no effect on the temporal signal.

In an experimental setting, a spectrum analyzer can measure the frequency broadening and the maximum phase shift can be extracted.

This broadening of the pulse spectra is what supercontinuum generators and frequency combs exploit.

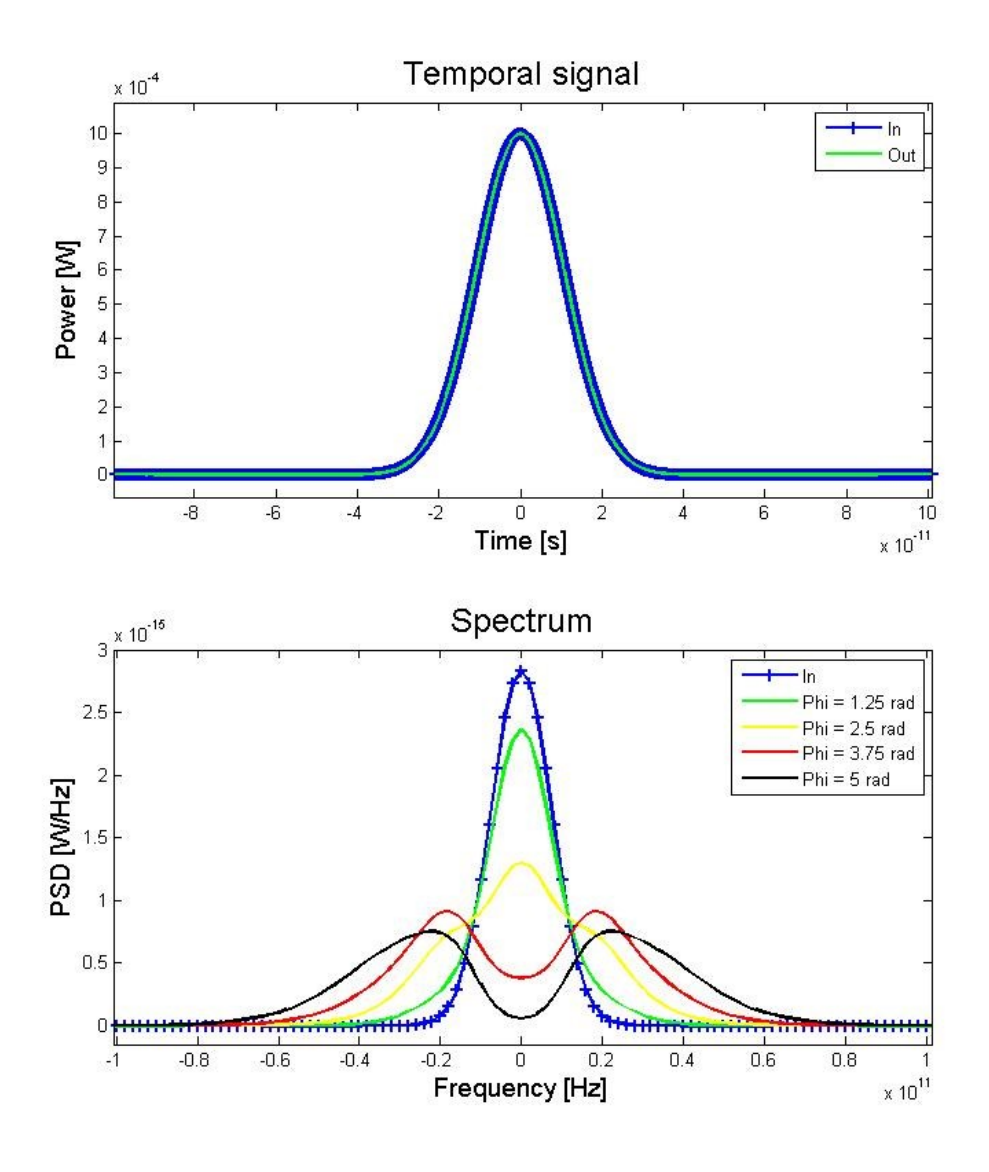


Figure 7: The change in time domain and frequency domain of a Gaussian pulse with maximum phase shift, Phi, of 1.25 rad, 2.5 rad, 3.75 rad and 5 rad. Taken from [25].

# **Chapter 4: Simulation of Finite Width Thin Film Gold Strip Waveguides**

In the preceding chapters, the theory behind surface plasmon polaritons and Kerr nonlinearity was introduced. This will be used later in this thesis to design the finite width gold strip waveguide, but for now the chosen method for simulating such a device will be discussed. The solution for a structure such as the one shown in Figure 8 cannot be found analytically, although there are plenty of numerical methods suitable for this problem, most notably the method of lines [11]. However, in this thesis the finite element method is implemented. The benefit of using a finite element method over the method of lines is that it can easily be adapted to complex geometries.

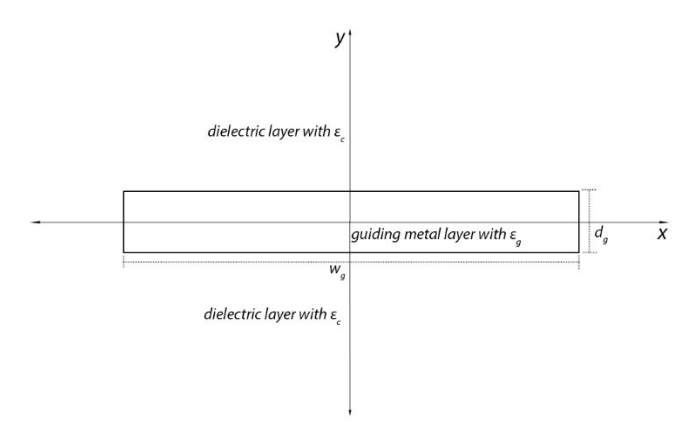


Figure 8: The structure of a finite width thin gold strip waveguide.

#### 4.1 The Vector Element Method

For an open waveguide problem as in Figure 8, traditional node-based finite element methods can introduce spurious solutions [26]. Furthermore, imposing boundary conditions on dielectric interfaces can be difficult and nodal elements also cause problems at edges and corners by creating field singularities [26].

Recently a new class of finite elements have emerged that do not introduce these difficulties; they are named vector elements [26]. Instead of using nodes, edges of elements are used as the degrees of freedom. Already it can be inferred that imposing boundary conditions should be much simpler.

In the vector element method, each element's edges are assigned a constant tangential field component. Then using proper basis functions, the vector field can be interpolated at any point inside the element. For a triangle element like the example in Figure 9, the vector field can be represented by three basis functions. Each basis function has a constant tangential field along its corresponding edge and vanishes at the opposite point. The normal field at each edge is not constant and so the vector field at each edge is not constant. This fact makes boundary conditions at dielectric and conducting interfaces trivial to enforce. At such interfaces the tangential field is continuous, whereas the normal fields are not.

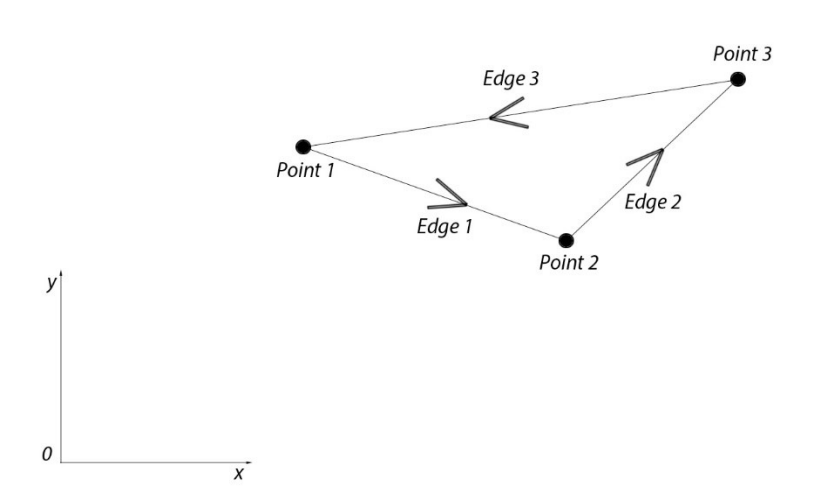


Figure 9: A typical triangular element with edges and points labelled counter clockwise.

The basis functions are derived in reference [26] and the vector field inside the element is given by equation (4.4) [26]. Bolded values are considered vectors.

$$N_1 = (L_1 \nabla L_2 - L_2 \nabla L_1) l_1 \tag{4.1}$$

$$N_2 = (L_2 \nabla L_3 - L_3 \nabla L_2) l_2 \tag{4.2}$$

$$\mathbf{N}_3 = (L_3 \nabla L_1 - L_1 \nabla L_3) l_3 \tag{4.3}$$

$$\boldsymbol{E} = \sum_{i=1}^{3} \boldsymbol{N}_{i} E_{i} \tag{4.4}$$

The basis functions contain,  $l_i$ , the side length and,  $L_i$ , the corresponding area coordinate. The area coordinate, used in conventional nodal analysis, is defined by

$$L_i = \frac{1}{b_1 c_2 - b_2 c_1} (a_i + b_i x + c_i y). \tag{4.5}$$

The area of the element,  $\Delta$ , is given by  $(b_1c_2 - b_2c_1)/2$ . The other variables  $a_i$ ,  $b_i$ , and  $c_i$  are defined by the three points that make up the triangular element.

$$a_{1} = x_{2}y_{3} - x_{3}y_{2} b_{1} = y_{2} - y_{3} c_{1} = x_{3} - x_{2}$$

$$a_{2} = x_{3}y_{1} - x_{1}y_{3} b_{2} = y_{3} - y_{1} c_{2} = x_{1} - x_{3} (4.6)$$

$$a_{3} = x_{1}y_{2} - x_{2}y_{1} b_{3} = y_{1} - y_{2} c_{3} = x_{2} - x_{1}$$

An example of the first edge's corresponding basis function is given by Figure 10. Notice that the field is zero at the opposite corner and the field lacks tangential components along edge 2 and edge 3.

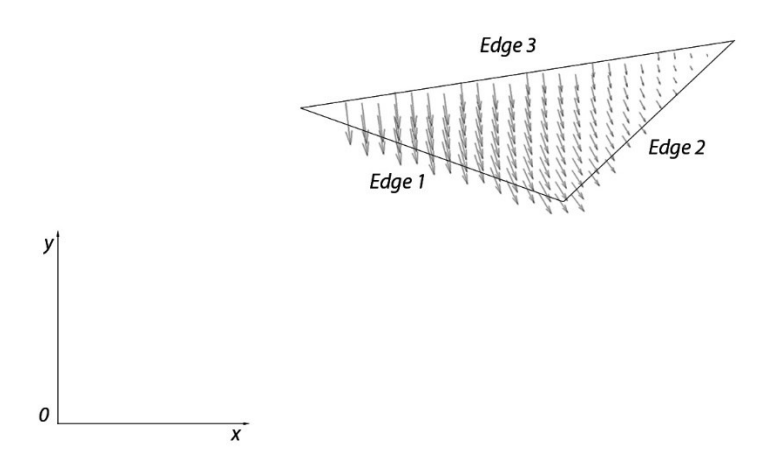


Figure 10: The basis function corresponding to edge 1, with vector quantities represented by arrows.

Now the electric field in a domain made up by these triangular elements can be approximated linearly by the basis functions.

#### 4.2 The Variational Method Formulation

The elements explained in the preceding section will be employed in the variational method for solving the propagation constants,  $\beta$ , of the waveguide in Figure 8. The

vector basis functions will be used to represent the transverse field on the simulation domain, whereas traditional node based elements will be implemented to represent the longitudinal field. Using [26] as a reference, the waveguide problem is described by the Helmholtz vector wave equation. The electric field is used here instead of the magnetic field because the boundary conditions are simpler to enforce.

$$\nabla \times (\nabla \times \mathbf{E}) - k_0^2 \varepsilon_r \mathbf{E} = 0 \tag{4.7}$$

Although this is an open waveguide problem, electric wall boundary conditions at sufficiently far finite distances are employed to simplify the derivation. For electric and magnetic wall boundaries, the conditions are as follows:

$$\hat{n} \times \mathbf{E} = 0$$
 for electric wall (4.8)

$$\hat{n} \times (\nabla \times \mathbf{E}) = 0$$
 for magnetic wall. (4.9)

Since the waveguide is lossy, the general variation principle is used to formulate the functional, and the inner product is defined as

$$\langle \phi | \psi \rangle = \int \phi \psi d\Omega. \tag{4.10}$$

The functional describing this problem is then given by equation (4.11) [26].

$$F(\mathbf{E}) = \frac{1}{2} \iint \left[ (\nabla \times \mathbf{E}) \cdot (\nabla \times \mathbf{E}) - k_0^2 \varepsilon_r \mathbf{E} \cdot \mathbf{E} \right] d\Omega \tag{4.11}$$

The transverse and longitudinal components of the electric field are broken up and the functional is given by equation (4.12). The complex propagation constant is now defined as  $\gamma = \alpha + j\beta$  with the z dependence  $E \sim e^{-\gamma z}$ [27].

$$F(\mathbf{E}) = \frac{1}{2} \iint \left[ (\nabla_t \times \mathbf{E}_t) \cdot (\nabla_t \times \mathbf{E}_t) - k_0^2 \varepsilon_r \mathbf{E} \cdot \mathbf{E} + (\nabla_t E_z + \gamma \mathbf{E}_t) \cdot (\nabla_t E_z + \gamma \mathbf{E}_t) \right] d\Omega$$

$$(4.12)$$

A change of variables is introduced to make solving for  $\gamma$  much easier [26].

$$\boldsymbol{e}_t = \gamma \boldsymbol{E}_t \tag{4.13}$$

$$e_z = E_z \tag{4.14}$$

The functional simplifies to equation (4.15) and agrees with reference [27].

$$F(\mathbf{E}) = \frac{1}{2} \iint \left[ (\nabla_t \times \mathbf{e}_t) \cdot (\nabla_t \times \mathbf{e}_t) - k_0^2 \varepsilon_r \mathbf{e}_t \cdot \mathbf{e}_t - \gamma^2 \left[ (\nabla_t e_z + \mathbf{e}_t) \cdot (\nabla_t e_z + \mathbf{e}_t) - k_0^2 \varepsilon_r e_z^2 \right] \right] d\Omega$$

$$(4.15)$$

Now the transverse and longitudinal field can be approximated in each element by edge and nodal elements, respectively. The first order nodal basis functions,  $N_i$ , are well-known and similar to the first order vector basis functions [26].

$$\mathbf{e}_{t}^{e} = \sum_{i=1}^{3} \mathbf{N}_{i}^{e} e_{ti}^{e} \tag{4.16}$$

$$e_z^e = \sum_{i=1}^3 N_i^e \, e_{zi}^e \tag{4.17}$$

The nodal basis functions are given by

$$N_i^e = \frac{1}{b_1 c_2 - b_2 c_1} (a_i + b_i x + c_i y); \tag{4.18}$$

in fact, they are equal to the area coordinates,  $L_i$ , stated earlier. Now the functional in matrix form can be expressed in terms of the basis functions. The vectors  $\{e_t^e\}$  and  $\{e_z^e\}$  represent the three edge and nodal values of each element with M total elements.

$$F(\mathbf{E}) = \frac{1}{2} \sum_{e=1}^{M} \left[ \{e_t^e\}^T A_{tt}^e \{e_t^e\} - \gamma^2 \begin{cases} e_t^e \\ e_z^e \end{cases}^T \begin{bmatrix} B_{tt}^e & B_{tz}^e \\ B_{zt}^e & B_{zz}^e \end{bmatrix} \begin{cases} e_t^e \\ e_z^e \end{cases} \right]$$
(4.19)

Each element has five corresponding symmetric elemental matrices. Later these matrices are added to the global matrices and the eigenvalue equation can be solved for  $\gamma$ .

$$A_{tt} = \iint \left[ (\nabla_t \times \mathbf{N}^e) \cdot (\nabla_t \times \mathbf{N}^e)^T - k_0^2 \varepsilon_r \mathbf{N}^e \cdot \mathbf{N}^{eT} \right] d\Omega \tag{4.20}$$

$$B_{tt} = \iint [\mathbf{N}^e \cdot \mathbf{N}^{e^T}] d\Omega \tag{4.21}$$

$$B_{tz} = \iint \left[ \mathbf{N}^e \cdot (\nabla_t N^e)^T \right] d\Omega \tag{4.22}$$

$$B_{zt} = \iint \left[ (\nabla_t N^e) \cdot \mathbf{N}^{eT} \right] d\Omega \tag{4.23}$$

$$B_{zz} = \iint \left[ (\nabla_t N^e) \cdot (\nabla_t N^e)^T - k_0^2 \varepsilon_r (N^e)^2 \right] d\Omega \tag{4.24}$$

Before progressing further, these integrals have to be solved. The reference [26] provides part of the solution for  $A_{tt}$  and  $B_{tt}$ .

$$\iint \left[ \left( \nabla_t \times \mathbf{N}_i^e \right) \cdot \left( \nabla_t \times \mathbf{N}_j^e \right) \right] d\Omega = \frac{l_i^e l_j^e}{\Delta^e}$$
 (4.25)

The solution for  $B_{tt}$  and the remaining component of  $A_{tt}$  is a bit more complex so the solution is put into a different form [26].

$$\iint \left[ \mathbf{N}_i^e \cdot \mathbf{N}_j^e \right] d\Omega = F_{ij}^e \tag{4.26}$$

$$f_{ij} = b_i b_j + c_i c_j \tag{4.27}$$

$$F_{11}^{e} = \frac{(l_1^{e})^2}{24\Delta^{e}} (f_{22} - f_{12} + f_{11})$$
 (4.28)

$$F_{12}^{e} = \frac{l_{1}^{e} l_{2}^{e}}{48\Delta^{e}} (f_{23} - f_{22} - 2f_{13} + f_{12})$$
(4.29)

$$F_{13}^{e} = \frac{l_{1}^{e} l_{3}^{e}}{48\Delta^{e}} (f_{21} - f_{11} - 2f_{23} + f_{13})$$
(4.30)

$$F_{22}^{e} = \frac{(l_2^{e})^2}{24\Delta^{e}} (f_{33} - f_{23} + f_{22})$$
 (4.31)

$$F_{23}^{e} = \frac{l_{2}^{e} l_{3}^{e}}{48\Delta^{e}} (f_{31} - f_{33} - 2f_{21} + f_{23})$$
 (4.32)

$$F_{33}^e = \frac{(l_3^e)^2}{24\Delta^e} (f_{11} - f_{13} + f_{33}) \tag{4.33}$$

Now the elemental matrices  $A_{tt}$  and  $B_{tt}$  can be given numerical values if  $\varepsilon_r$  is assumed to be constant within each element. Contrary to the reference [26],  $\mu_r$  is assumed to be unity for the entire simulation domain.

$$A_{tt} = \frac{l_i^e l_j^e}{\Delta^e} - k_0^2 e_r F_{ij}^e \tag{4.34}$$

$$B_{tt} = F_{ij}^e (4.35)$$

The remaining three matrices can be solved by using the equations (4.30) and (4.33) from the reference [26]. For equation (4.36), i + 1 takes on the value of 1 when i = 3.

$$B_{tz} = \frac{l_i^e}{12\Delta^e} \left( b_{i+1}b_j + c_{i+1}c_j - b_ib_j - c_ic_j \right)$$
 (4.36)

From the symmetry of the elemental matrices,  $B_{zt}$  can be found by taking the transpose of  $B_{tz}$ .

$$B_{zt} = B_{tz}^{T} (4.37)$$

Finally  $B_{zz}$  is given by equation (4.38), where  $\delta_{ij}$  is the Kronecker delta.

$$B_{zz} = \frac{f_{ij}}{4\Delta^e} - k_0^2 \varepsilon_r \frac{\Delta^e}{12} (1 + \delta_{ij})$$
 (4.38)

Now that all of the elemental matrices have been defined, the functional problem can be rewritten using global notation. Since each edge is usually shared by adjacent elements, the direction of the edge element will be defined in opposite directions. When constructing the global matrix, it is important to choose a global direction so that the simulation program knows to either add or subtract the contribution of a different elemental matrix. This problem does not arise for the scalar nodal contributions and they are simply added. The functional problem is now expressed by equation (4.39).

$$F(\mathbf{E}) = \frac{1}{2} \left[ \{e_t\}^T A_{tt} \{e_t\} - \gamma^2 \begin{Bmatrix} e_t \\ e_z \end{Bmatrix}^T \begin{bmatrix} B_{tt} & B_{tz} \\ B_{zt} & B_{zz} \end{Bmatrix} \begin{Bmatrix} e_t \\ e_z \end{Bmatrix} \right]$$
(4.39)

Finally the functional can be reduced to a generalized eigenvalue problem as seen in reference [26]. The only difference is the lack of a minus sign, which is a result of using the generalized variational principle and removal of the complex conjugate operators.

$$\begin{bmatrix} A_{tt} & 0 \\ 0 & 0 \end{bmatrix} \begin{Bmatrix} e_t \\ e_z \end{Bmatrix} = \gamma^2 \begin{bmatrix} B_{tt} & B_{tz} \\ B_{zt} & B_{zz} \end{bmatrix} \begin{Bmatrix} e_t \\ e_z \end{Bmatrix}$$
(4.40)

These matrices are extremely sparse and symmetric. Built in functions for MATLAB can solve these problems easily with an initial guess. The dispersion equations from **Chapter 2: Plasmon Polariton Waves** can be used to supply the prerequisite initial guess, since the waveguides are much wider than they are thick.

As an example and validation of this technique, results were reproduced from "Finite element analysis of lossy dielectric waveguides" [27]. The propagation constant of the metal-insulator-semiconductor transmission line in [27] was solved and Figure 5 and Figure 6 from [27] were reproduced. They are in good agreement with the reproduced results in Figure 11 and Figure 12.

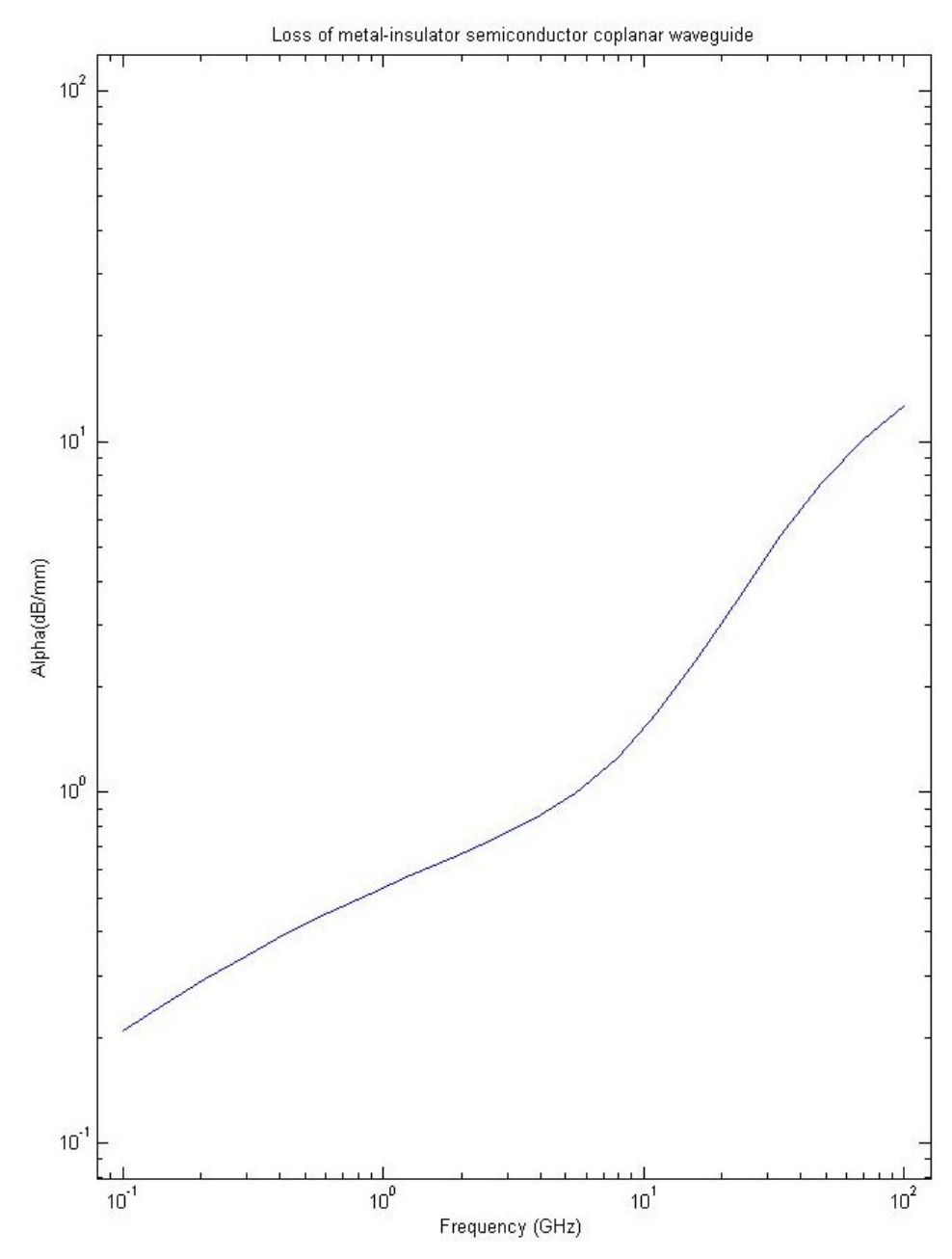


Figure 11: Reproduction of loss results for MIS-CPW, simulated in MatLab.

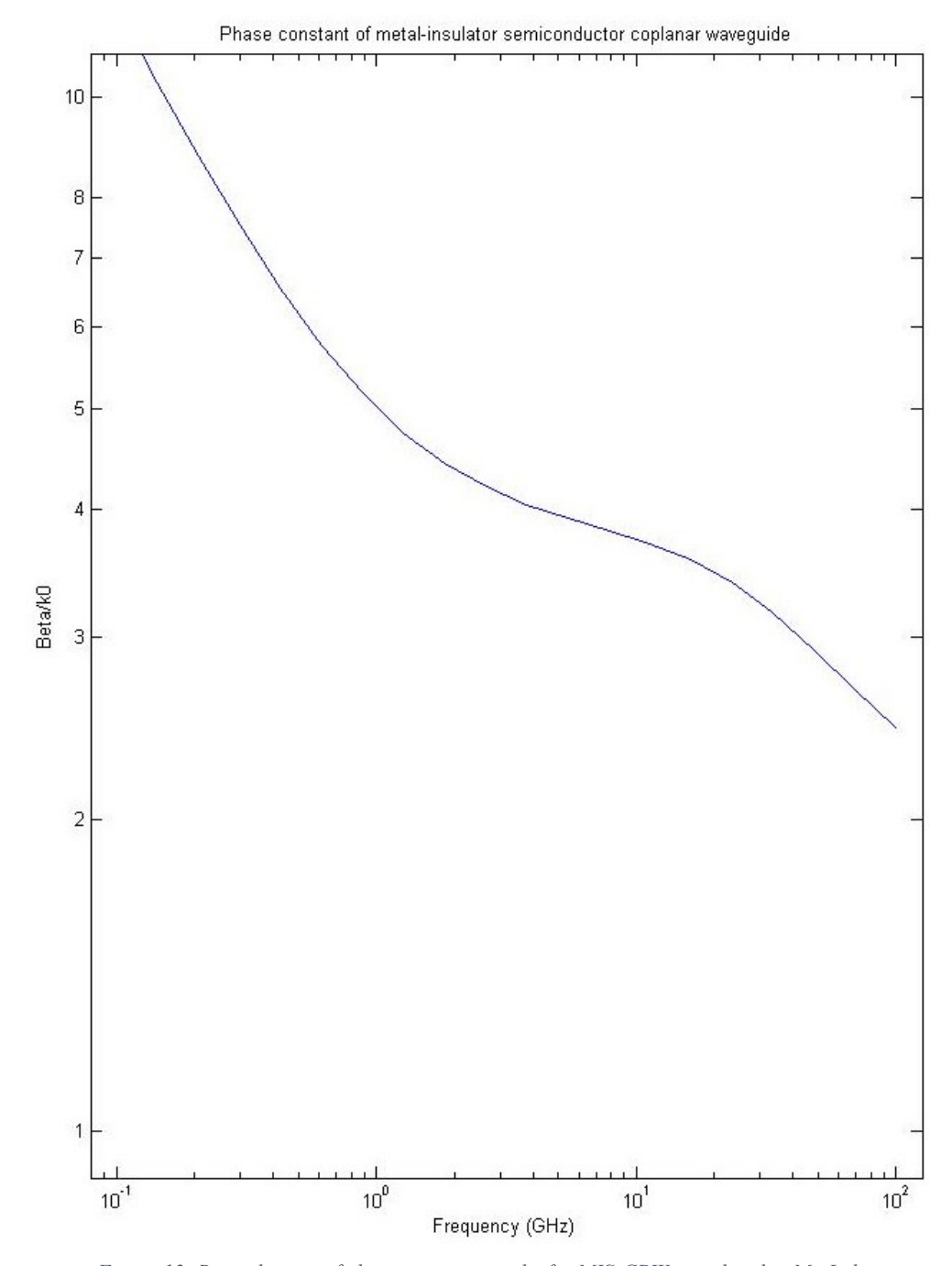


Figure 12: Reproduction of phase constant results for MIS-CPW, simulated in MatLab

## 4.3 Simulation of Chalcogenide Gold Strip Waveguides

The simulation technique was tested by demonstrating its convergence as the number of triangular elements was increased, as shown in Figure 13.

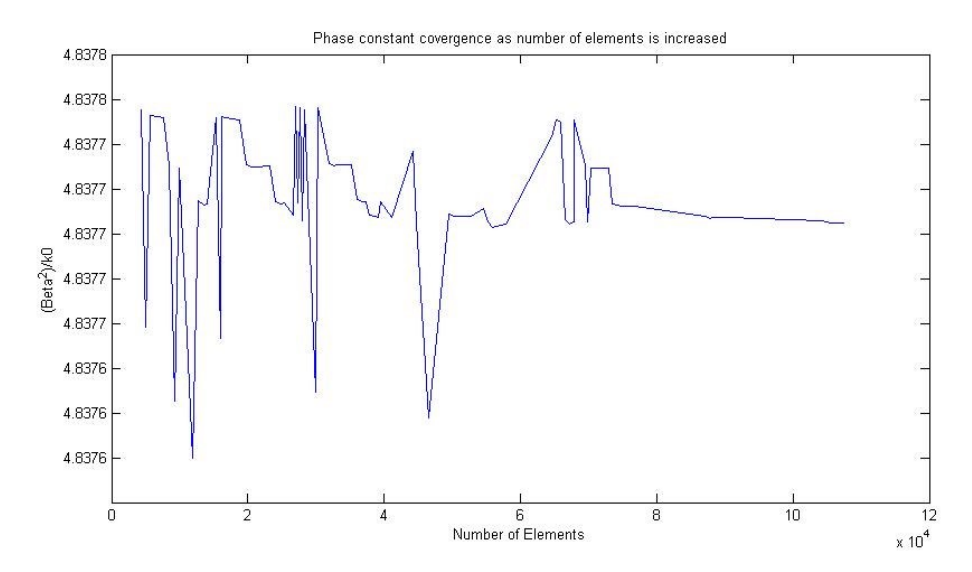


Figure 13: Convergence of the phase constant as the number of elements is increased. Simulated in MatLab.

Two methods of increasing the number of elements were used. First the number of triangles was increased along the edges of the gold film because the electric field varies very quickly near and inside metals. Then the maximum element size was also decreased in steps. The structure simulated was a 10 nm thick 3  $\mu$ m wide gold film encased in Chalcogenide glass. To improve the accuracy of the simulation, the Chalcogenide glass was not assumed to be infinitely thick. Instead the glass was given a 4  $\mu$ m thickness below the film and a 5  $\mu$ m thickness above the gold film, an artifact of the fabrication process. The simulation domain then included both the soda lime substrate and surrounding air with  $\epsilon_{sub} = 2.25$  and  $\epsilon_{air} = 1$ .

Furthermore, the symmetry of the structure was used to halve the simulation domain, and electric wall boundary conditions were used for top, right and bottom simulation edges. The remaining left edge was given the magnetic wall boundary condition so that only symmetric modes would be calculated.

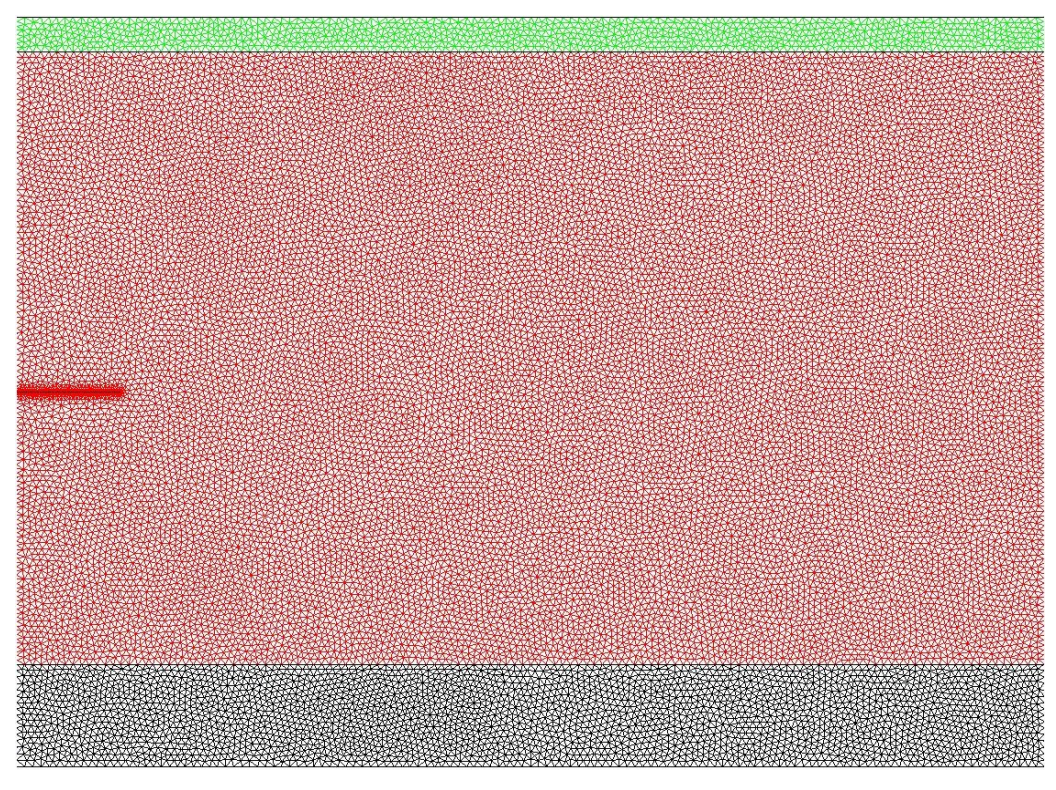


Figure 14: Mesh of simulation domain. Red represents the Chalcogenide glass, black represents the soda lime substrate and green represents the air. Simulated using MatLab.

The gold film is hard to discern since it is very small compared to the mode size. However, the densely populated region at the center left gives away its position. The mode was found by giving an initial estimate slightly larger than the electric permittivity of the Chalcogenide glass. Then the next five modes with the largest values for the phase constant were compared. The lowest order ss mode was easily found by comparing the real part of the phase constant or loss. Modes that would be considered sa have much larger losses and field confinement than the ss modes. Finally, non-physical modes that appear due to the electric wall boundary conditions were removed because of their very low loss characteristics. The electric field profile can be calculated to confirm the presence of the ss mode. According to [11], the ss mode should have a very small  $E_x$  component. The  $E_y$  component should be symmetric and the dominant field. Furthermore, for very thin films, as in this case, the field should be similar to the fundamental mode of an optical fiber. The following figures give the spatial field distribution of the three electrical field components over half of the actual geometry at an illumination wavelength of 1550

nm. As expected, the  $E_y$  component is the dominant field and the  $E_x$  is zero everywhere except for the corners of the gold film. The phase constant, normalized by the wavenumber  $k_0$ , was found to be 2.1995. The loss calculated from the propagation constant was 4.5354 dB/cm.

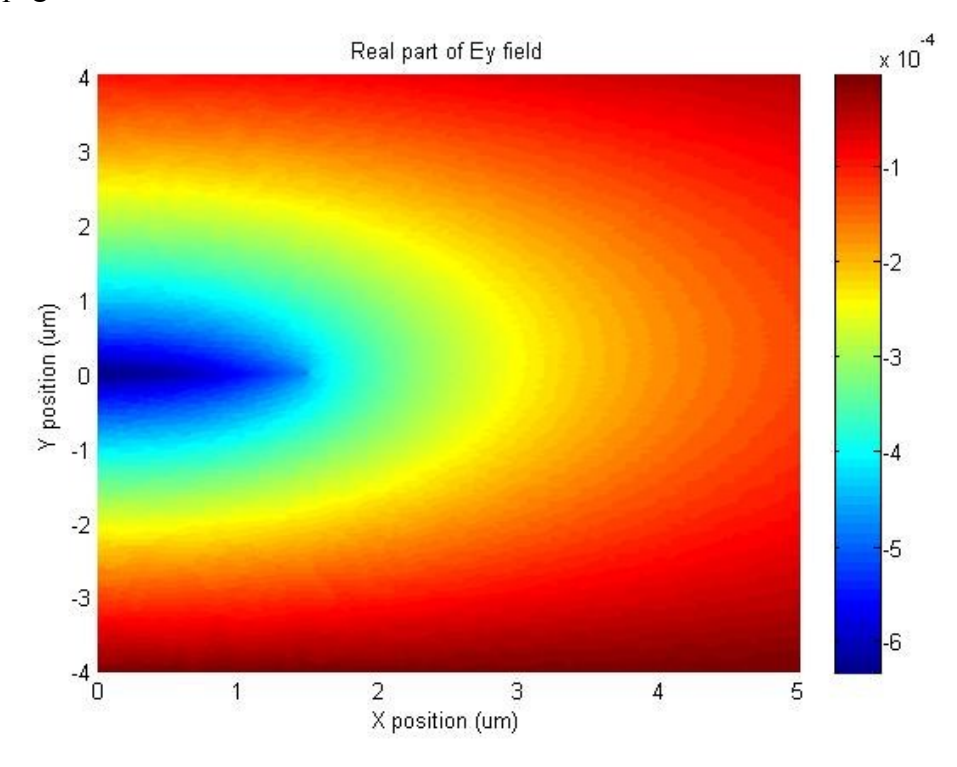


Figure 15: E<sub>y</sub> field of the lowest order ss mode of the gold film plasmon polariton waveguide. Simulated using MatLab

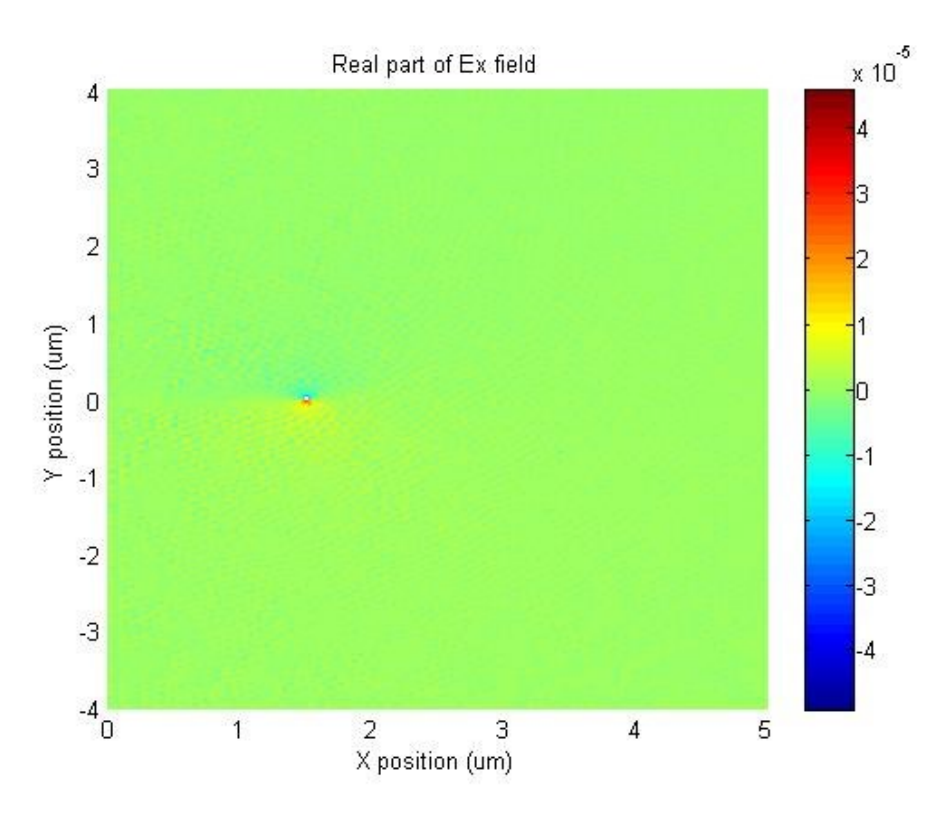


Figure 16:  $E_x$  field of the lowest order ss mode of the gold film plasmon polariton waveguide. Simulated using MatLab.

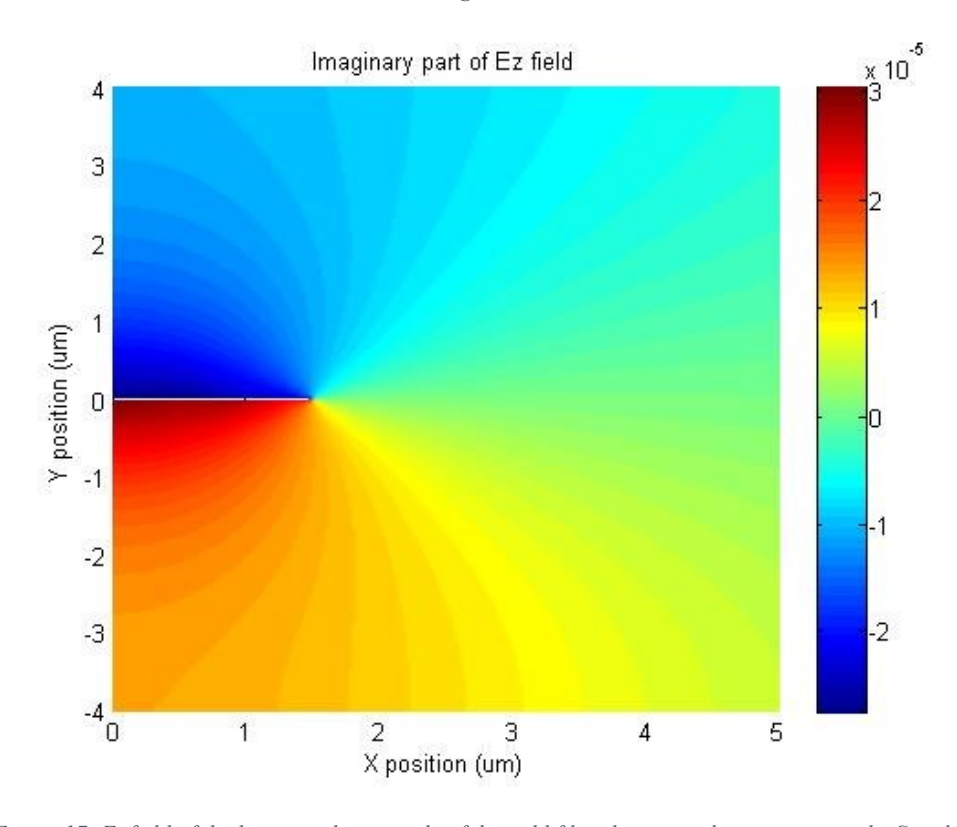


Figure 17:  $E_z$  field of the lowest order ss mode of the gold film plasmon polariton waveguide. Simulated using MatLab.

## 4.4 Optimization of Chalcogenide Gold Strip Waveguide Design

There are two key parameters to consider when designing a waveguide that maximizes the amount of nonlinear phase shift of a pulse. They are the loss and the effective area of the mode. Increasing loss lowers the effective length in equation (3.20) and a larger effective area increases the nonlinear length,  $L_{NL}$ , in the same equation.

From the properties of the ss mode, the loss and effective area can be changed by increasing or decreasing the thickness and width of the gold film. For this design, the correct thickness and width of the gold film must be chosen carefully to minimize the loss and minimize the effective area. To this end, a couple of different simulations were run to compare the value of  $L_{eff}$  and  $A_{eff}$  for different waveguide transverse dimensions. From equation (3.20), it is evident that having a large effective length and small nonlinear length increases the amount of phase shift. Thus, the optimized waveguide will have the largest figure of merit. The nonlinear phase shift can then be calculated with this ratio and using equation (4.41). The values reported in Table 2 are for waveguides with infinite lengths.

$$\Delta \varphi_{max} = k_0 n_2^I P_{Max} \frac{L_{eff}}{A_{eff}} \tag{4.41}$$

Titux	$A_{eff}$	( ' )

	Width 2.5 μm	Width 3 µm	Width 3.5 μm	Width 4 µm
Thickness 8 nm	0.0029 W <sup>-1</sup>	0.0026 W <sup>-1</sup>	0.0024 W <sup>-1</sup>	0.0022 W <sup>-1</sup>
Thickness 10 nm	0.0020 W <sup>-1</sup>	0.0019 W <sup>-1</sup>	0.0017 W <sup>-1</sup>	0.0016 W <sup>-1</sup>
Thickness 12 nm	0.0015 W <sup>-1</sup>	0.0014 W <sup>-1</sup>	0.0013 W <sup>-1</sup>	0.0012 W <sup>-1</sup>
Thickness 14 nm	0.0012 W <sup>-1</sup>	0.0011 W <sup>-1</sup>	0.0010 W <sup>-1</sup>	0.00094 W <sup>-1</sup>

Table 2: Comparison of the figures of merit for waveguides with different width and thickness characteristics.

The figure of merit increases as the thickness and width decrease, this is a result of lowering losses of the waveguides. In this thesis, waveguides of 1 cm were fabricated, so the table is updated to reflect the different effective lengths. The results can be found in Table 3.

Table 3: Comparison of the figures of merit for waveguides with length of 1 cm.

	Width 2.5 μm	Width 3 µm	Width 3.5 µm	Width 4 µm
Thickness 8 nm	0.0010 W <sup>-1</sup>	0.0011W <sup>-1</sup>	0.0012 W <sup>-1</sup>	0.0012 W <sup>-1</sup>
Thickness 10 nm	0.0012 W <sup>-1</sup>	0.0012 W <sup>-1</sup>	0.0012 W <sup>-1</sup>	0.0012 W <sup>-1</sup>
Thickness 12 nm	0.0012 W <sup>-1</sup>	0.0012 W <sup>-1</sup>	0.0011 W <sup>-1</sup>	0.0011 W <sup>-1</sup>
Thickness 14 nm	0.0011 W <sup>-1</sup>	0.0010 W <sup>-1</sup>	0.00098 W <sup>-1</sup>	0.00092 W <sup>-1</sup>

From Table 3, the waveguides with the highest figure of merit have a thickness of 10 nm. The best candidate with a width of 3  $\mu$ m and thickness 10 nm had an effective area of 36  $\mu$ m<sup>2</sup>. Since this waveguide has a large effective area, it is better suited to butt coupling with a single mode optical fiber and is the better choice. However, during the process of fabrication, waveguides with widths 3  $\mu$ m and up were fabricated and their loss characteristics were analyzed.

Using these results, an estimate for the amount of nonlinear phase shift that a pulse accumulates over 1 cm of propagation can be calculated. Using an  $n_2$  of  $1.7 \times 10^{-6}$   $\mu m^2/W$  provided by [28], the phase shift is calculated as 0.0012 radians · W<sup>-1</sup>. The value,  $n_2$ , of Ge<sub>23</sub>Sb<sub>7</sub>S<sub>70</sub> is given at the wavelength 1064 nm, whereas this thesis is interested in the wavelength regime of 1550 nm. According to [28], this value is different at 1550 nm but it at least gives an estimate for the correct value. For a pulse power of 1 kW, the phase shift of the pulse should be close to 1 radian. This phase shift is quite low for such a high pulse power and in fact, higher phase shifts can be achieved by using Chalcogenide micro wires as in [14]. It appears that the trade-off between field confinement and propagation loss for the ss mode is too restricting to achieve a good result.

## 4.5 Calculation of Coupling Coefficient Between SMF 28 and Plasmon Polariton Waveguide

To test the loss characteristics of the gold strip waveguide, SMF 28 fiber was used to couple light in an end fire configuration. Since the spatial distribution of the *ss* mode is similar to the fundamental mode of the fiber, a good coupling efficiency

was expected. To get a clearer answer to the loss, the coupling efficiency was calculated by equation (4.42) [29], [30].

$$\eta = Re \left( \frac{\int (\mathbf{E}_{SMF} \times \mathbf{H}_{SPW}^*) \cdot d\mathbf{A} \int (\mathbf{E}_{SPW} \times \mathbf{H}_{SMF}^*) \cdot d\mathbf{A}}{\int (\mathbf{E}_{SMF} \times \mathbf{H}_{SMF}^*) \cdot d\mathbf{A} \int (\mathbf{E}_{SPW} \times \mathbf{H}_{SPW}^*) \cdot d\mathbf{A}} \right)$$
(4.42)

In the equation, *SMF* stands for the single mode fiber fundamental mode fields and *SPW* stands for the fields of the *ss* mode in the plasmon polariton waveguide. This equation does not take into account minor defections in the waveguide facets or translational and angular misalignment between waveguides.

There is also a small difference between the effective indices of both the fiber and plasmon polariton waveguide. This is taken into account by equation (4.43).

$$T = \frac{4n_{SMF}^{eff}n_{SPW}^{eff}}{\left(n_{SMF}^{eff} + n_{SPW}^{eff}\right)^2} \tag{4.43}$$

The single mode fiber supports two polarizations and thus supports two modes. The gold strip waveguide however, only supports one of these polarizations. This causes the observed loss to increase by a factor of 2, since one of the polarizations will not couple to the ss mode of the plasmon polariton waveguide. The total estimated loss,  $L_{tot}$ , for a single coupling between single mode fiber and gold strip waveguide is then given by

$$\boldsymbol{L}_{tot} = \frac{1}{2}T\eta. \tag{4.44}$$

Using the results obtained from the finite element method, the loss for the 3  $\mu$ m wide and 10 nm thick waveguide was found to be  $L_{tot} = 0.42$  or 3.7 dB. These simulation results show that this structure could be a good candidate for coupling light from single mode fibers.

# **Chapter 5: Fabrication and Experimentation of Gold Strip Waveguides**

### **5.1** Fabrication Process

To construct a waveguide that can easily support the *ss* mode, the geometry must be symmetric on the *x* axis, or according to Figure 18, symmetric vertically. Theoretically, it is possible to support an *ss* mode on an asymmetric waveguide, but if not designed properly all the *ss* modes can be cut off [31]. Furthermore, the fabrication process made the use of some Chalcogenides impossible. As<sub>2</sub>Se<sub>3</sub> has a very high nonlinear index of refraction, yet it could not be used because it is attacked by common photolithography developer solutions [32]. The fabrication process is explained by Figure 18. A similar fabrication example can found in [33].

First a 4  $\mu$ m film of Chalcogenide glass was deposited on a soda lime substrate. Soda lime with its low index of refraction was used so that light would not be guided out of the main waveguide. Then following [33], resist was deposited and patterned. To construct the gold strips, gold was first deposited and then a gold liftoff process was performed.

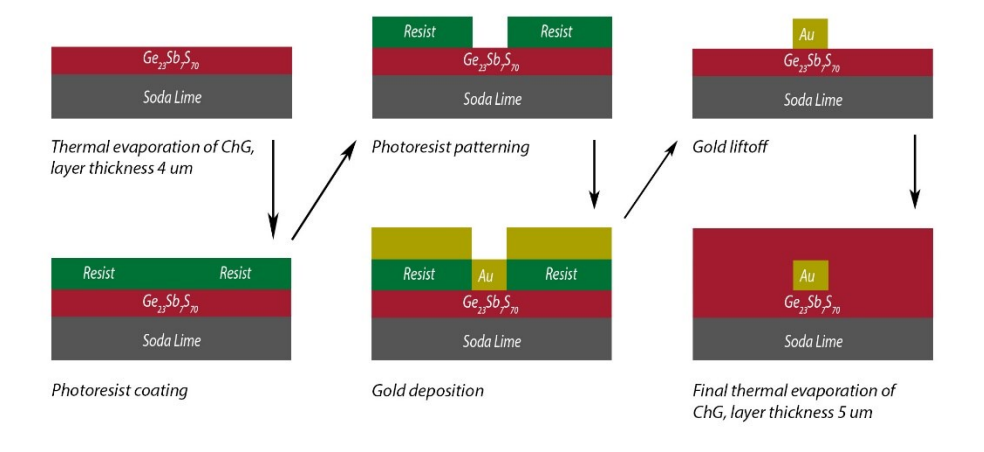


Figure 18: Fabrication steps to construct gold strip plasmon polariton waveguides. The diagrams are given from the transverse plane.

Finally, the structure was completed with a 5  $\mu$ m film of Chalcogenide. The photomask used in the patterning had many different dimensions for length and width. There was a 3  $\mu$ m minimum feature size constraint on the width, but structures up to 20  $\mu$ m wide were patterned. To better measure the loss 0.5 cm, 1 cm and 2 cm were patterned as well.

These fabrication steps, most notably the thermal evaporation of the Chalcogenide glass, were made possible by a collaboration with Prof. Juejun Hu at the University of Delaware.

The last fabrication step remaining was to mechanically dice the soda lime substrate so that an optical fiber could be end fire coupled to the waveguides. Achieving a smooth end facet for the waveguide proved very difficult.

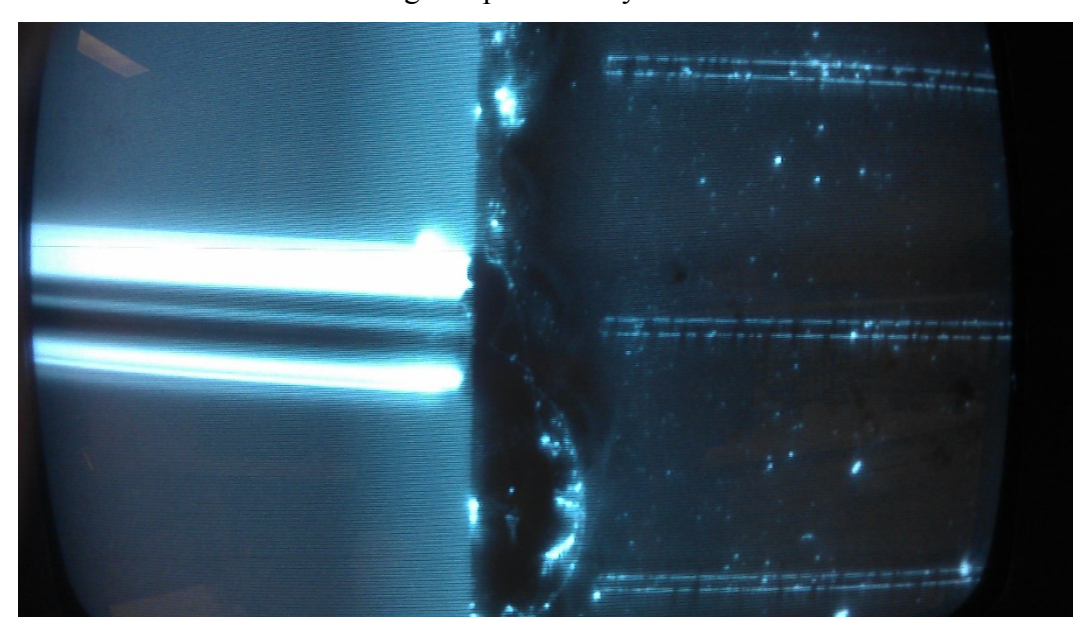


Figure 19: Facets after mechanical dicing. The dicing was a distance away from the gold strips for a better result. A cleaved SMF is shown on the left.

The results of the dicing are displayed in Figure 19. A cleaved single mode fiber is shown to the left of the soda lime substrate and the waveguides can be seen on the right with widths of approximately 5 µm. Significant chipping of the top layers of glass can easily be seen from this picture. When the dicing was moved closer to the gold strips, the facets were worse. It appears that the gold layers would strip away the thin films of Chalcogenide glass as seen in Figure 20. The soda lime substrate

however had a much straighter and smoother edge. In a similar type of structure, much smoother end facets were achieved, even before any polishing [34]. Thus, either the fabrication method or material system should be changed for a better dicing result.



Figure 20: The dicing was moved closer to the waveguides and the results were much worse. The two layers of Chalcogenide glass can be seen chipped away at different positions. The gold layers are stripped much farther back from the edge.

## 5.2 Loss Experimentation on Plasmon Polariton Waveguides

Even though the results of the dicing were not perfect and large losses were expected, the waveguides' loss characteristics were analyzed.



Figure 21: Experimental setup of loss experiment.

First, an erbium doped fiber amplifier (EDFA) was used as a broad band source, which was coupled to the samples by a single mode fiber. The signal was then coupled through another fiber to an optical spectrum analyzer (OSA) to determine the losses and its dependence on wavelength. Figure 22 shows the coupling setup between the single mode fibers and the sample. This setup along with the

microscope provided fine control of the lateral position. Without a camera to check the vertical position of the fibers, it was difficult to get a precise vertical position of the fibers. This was overcome by incrementally lowering both fibers until a signal was received.

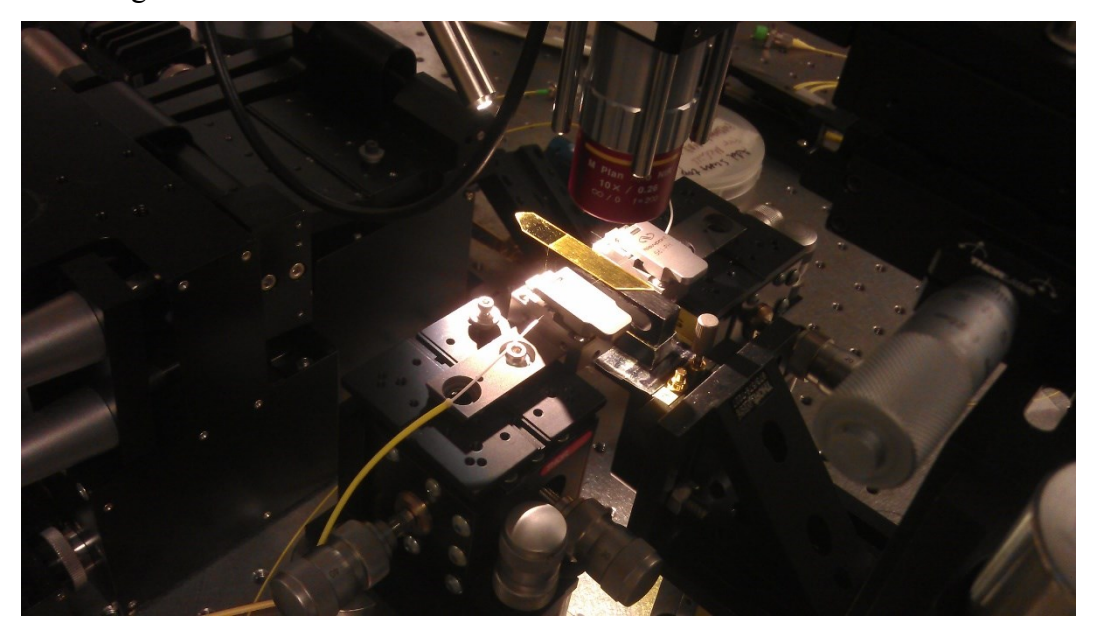


Figure 22: The setup for coupling light in and out of the plasmon polariton waveguides (center). Translational stages were used on the two fiber clamps and the microscope to have better control of the coupling.

## **Chapter 6: Results and Conclusion**

## **6.1** Results of Loss Experiment

The waveguides with the cleanest end facets were used to calculate the loss from the coupling and propagation of the signal. There was significant glass chipping on the 5  $\mu$ m and 6  $\mu$ m wide waveguides and their results were not included. An input signal of 5 mW was launched into the fibers and collected at the output with the OSA, as shown in Figure 23. The resolution bandwidth was set to 0.1 nm to adequately distinguish power levels between wavelengths. The sensitivity of the OSA was set to 80 dBm and accounts for the noisy signal data in high loss wavelengths.

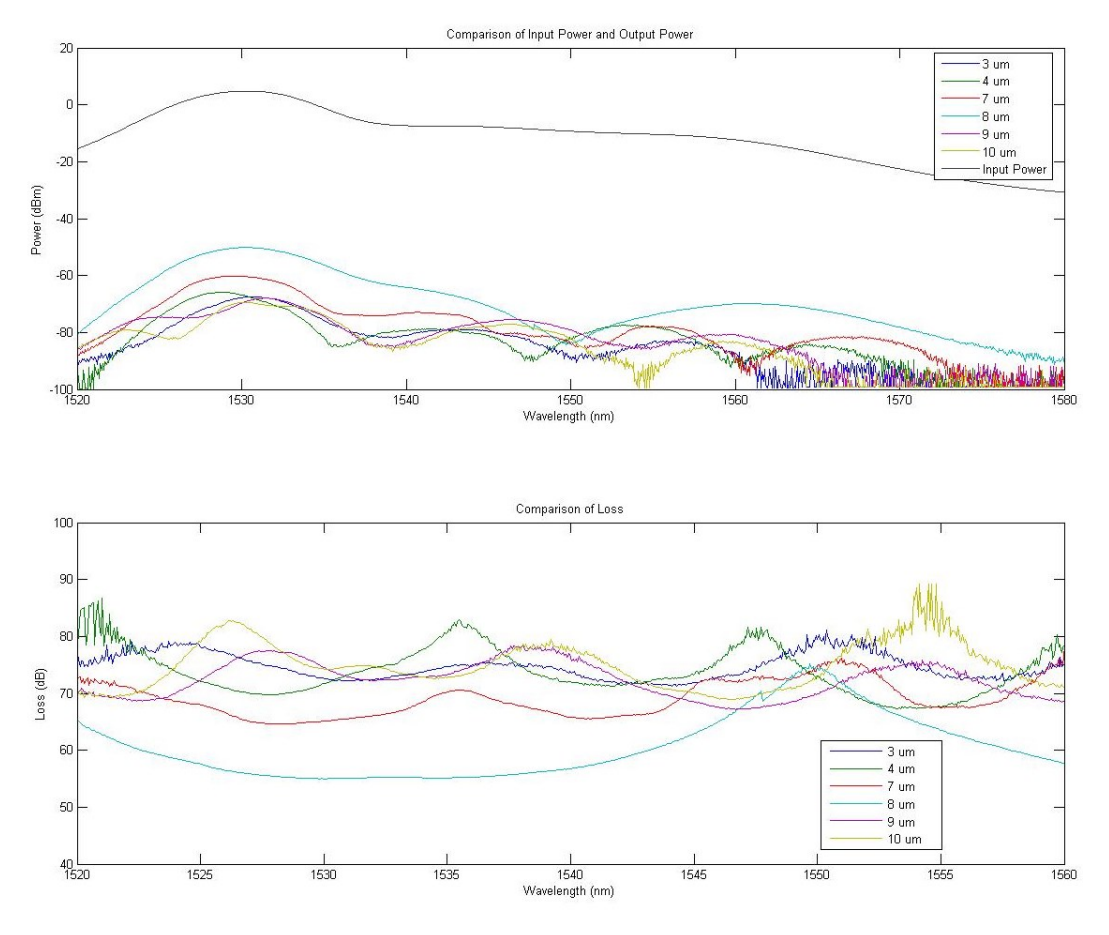


Figure 23: Loss measurement of plasmon polariton waveguide.

The loss was much higher than theoretically predicted, assuming a perfectly flat facet for the waveguides. At 1550, after a fiber-waveguide coupling, 3.7 dB loss, 1 cm of propagation, 4.54 dB of loss, and finally another fiber-waveguide coupling, 3.7 dB loss, the total loss should have been 11.94 dB. Instead, the observed loss at 1550 nm for a 3 µm wide waveguide was found to be approximately 75 dB. This high loss most likely resulted from the field not being coupled well with the waveguide. The chipped facets and the distance of the fibers from the waveguides increased the loss dramatically. It is difficult to interpret these results because of the high losses most likely caused by scattering at the facets. The origin of the dips in transmission are not well understood because it is difficult to know whether the light was successfully coupled to the waveguides or if it had simply radiated through the Chalcogenide glass layers.

## 6.2 Conclusion

In this thesis, a method for increasing the nonlinear phase shift using surface plasmon polaritons was introduced. The tangential finite element method proved a strong and accurate tool for simulating and calculating the propagating modes of a finite width thin film structure. Using surface plasmon polariton modes of a finite width thin film waveguide, light can be confined to a smaller effective area. This is a useful tool in enhancing the nonlinear phase shift. Unfortunately, for this material structure and basic rectangular geometry, the trade-off between loss and field confinement of the *ss*<sup>0</sup> mode is too stringent and the result of 0.0012 rad·W<sup>-1</sup> for 1 cm propagation is much lower than results obtained for Chalcogenide micro wires [14]. However, the coupling loss was calculated between an SMF fundamental mode and the *ss* mode and it had a low value of 3.7 dB. The figure of merit and waveguide nonlinear coefficient for this device is compared to other waveguide types in Table 4. The final figure of merit is quite low compared to the other waveguide types and is attributed to its loss characteristics.

Table 4: A comparison of the figure of merit for the surface plasmon polariton.

Waveguide type	Nonlinear index $n_2$ (m <sup>2</sup> /W)	Nonlinear coefficient γ (W <sup>-1</sup> ·m <sup>-1</sup> )	Loss α (dB/m)	Effective length L <sub>eff</sub> (m)	Nonlinear figure of merit (FOM) $\gamma \cdot L_{eff}(W^{-1})$
Highly nonlinear silica fiber [16]	2.2×10 <sup>-20</sup>	0.021	0.2	21715	91.20
Bismuth oxide fiber (Bi <sub>2</sub> O <sub>3</sub> ) [17],[18]	1.1×10 <sup>-18</sup>	1.36	0.8	5.42	7.38
As <sub>2</sub> S <sub>3</sub> waveguide [5]	3.0×10 <sup>-18</sup>	9.9	60	0.072	0.72
Silicon waveguide [19], [20]	4.5×10 <sup>-18</sup>	150	400	0.011	1.63
As <sub>2</sub> Se <sub>3</sub> [14]	1.1×10 <sup>-17</sup>	187	<1	4.343	812.14
Ge <sub>23</sub> Sb <sub>7</sub> S <sub>70</sub> surface plasmon polariton waveguide	1.7×10 <sup>-18</sup>	0.194	453.5	0.0096	0.0019

Theoretically, this structure could be used in a future plasmon polariton setup as an intermediary between some plasmon polariton structure and a single mode fiber. This value for loss could be lowered even more by tailoring the width and thickness of the gold strip to produce a mode much more similar to the SMF fundamental mode.

The loss experiment was conducted but without a cleaner end facet, the correct loss characteristics could not be determined. This might be due to an issue with the relatively thick thermally evaporated films chipping easily as the sample was diced.

### **6.3** Future Work

In future projects with Chalcogenide surface plasmon polaritons, researchers should use a different dicing procedure or a different crystalline substrate that can be easily cleaved, such as Silicon. Another option is to attempt a different deposition technique for the Chalcogenide layers, as in [32], where the Chalcogenide is deposited by solution processing. This has the added benefit of including other Chalcogenides (e.g., As<sub>2</sub>Se<sub>3</sub> that have a much higher nonlinear index. Solution processing also has the ability to deposit thick layers easily.

Other geometries could be attempted to investigate their loss to field confinement characteristics as in [35]. It was also observed that introducing the lower refractive index layers above and below the Chalcogenide layers provided extra field confinement because the layers behaved like a slab dielectric waveguide. When investigating future geometries, a study of combining dielectric confinement with the surface plasmon polariton mode could be fruitful. Since the *ss*<sup>0</sup> mode is very similar to the fundamental mode of an optical fiber, over short distances a fiber implanted with a metal strip could be made a true single mode fiber that supports only a single linear polarization.

## References

- [1] J. B. Khurgin and G. Sun, "Plasmonic enhancement of the third order nonlinear optical phenomena: Figures of merit," *Opt. Express*, vol. 21, no. 22, p. 27460, Nov. 2013.
- [2] T. Kamiya and M. Tsuchiya, "Progress in Ultrafast Photonics," *Jpn. J. Appl. Phys.*, vol. 44, no. 8, pp. 5875–5888, Aug. 2005.
- [3] T. a Birks, W. J. Wadsworth, and P. S. Russell, "Supercontinuum generation in tapered fibers.," *Opt. Lett.*, vol. 25, no. 19, pp. 1415–7, Oct. 2000.
- [4] U. Keller, "Recent developments in compact ultrafast lasers.," *Nature*, vol. 424, no. 6950, pp. 831–8, Aug. 2003.
- [5] M. R. Lamont, B. Luther-Davies, D.-Y. Choi, S. Madden, and B. J. Eggleton, "Supercontinuum generation in dispersion engineered highly nonlinear (gamma = 10 /W/m) As2S3) chalcogenide planar waveguide.," *Opt. Express*, vol. 16, no. 19, pp. 14938–44, Sep. 2008.
- [6] Y. Okawachi, A. L. Gaeta, and M. Lipson, "Breakthroughs in Nonlinear Silicon Photonics 2011," *IEEE Photonics J.*, vol. 4, no. 2, pp. 601–606, Apr. 2012.
- [7] Q. Liu, X. He, X. Zhao, F. Ren, X. Xiao, C. Jiang, X. Zhou, L. Lu, H. Zhou, S. Qian, B. Poumellec, and M. Lancry, "Enhancement of third-order nonlinearity in Ag-nanoparticles-contained chalcohalide glasses," *J. Nanoparticle Res.*, vol. 13, no. 9, pp. 3693–3697, Feb. 2011.
- [8] K. Fukumi, A. Chayahara, K. Kadono, T. Sakaguchi, Y. Horino, M. Miya, K. Fujii, J. Hayakawa, and M. Satou, "Gold nanoparticles ion implanted in glass with enhanced nonlinear optical properties," *J. Appl. Phys.*, vol. 75, no. 6, p. 3075, 1994.
- [9] R. F. Haglund, L. Yang, R. H. Magruder Iii, J. E. Wittig, K. Becker, and R. a Zuhr, "Picosecond nonlinear optical response of a Cu:silica nanocluster composite.," *Opt. Lett.*, vol. 18, no. 5, pp. 373–5, Mar. 1993.
- [10] H. B. Liao, R. F. Xiao, H. Wang, K. S. Wong, and G. K. L. Wong, "Large third-order optical nonlinearity in Au:TiO[sub 2] composite films measured on a femtosecond time scale," *Appl. Phys. Lett.*, vol. 72, no. 15, p. 1817, 1998.

- [11] P. Berini, "Plasmon-polariton waves guided by thin lossy metal films of finite width: Bound modes of symmetric structures," *Phys. Rev. B*, vol. 61, no. 15, pp. 10484–10503, Apr. 2000.
- [12] A. Huck, D. Witthaut, S. Kumar, A. S. Sørensen, and U. L. Andersen, "Large Optical Nonlinearity of Surface Plasmon Modes on Thin Gold Films," *Plasmonics*, vol. 8, no. 4, pp. 1597–1605, Jun. 2013.
- [13] J. Hu, "Planar Chalcogenide Glass Materials and Devices," Ph.D. dissertation, Dept. Mater. Sci. Eng., MIT, Cambridge, MA, 2009.
- [14] C. Baker, "Hybrid As2Se3-PMMA Microtapers and Applications," Ph.D. dissertation, Dept. Elect. Comp. Eng., McGill Univ., Montreal, QC, 2013.
- [15] J. D. Musgraves, N. Carlie, J. Hu, L. Petit, A. Agarwal, L. C. Kimerling, and K. a. Richardson, "Comparison of the optical, thermal and structural properties of Ge–Sb–S thin films deposited using thermal evaporation and pulsed laser deposition techniques," *Acta Mater.*, vol. 59, no. 12, pp. 5032–5039, Jul. 2011.
- [16] G. Agrawal, *Nonlinear Fiber Optics*, 5th ed. Rochester: The Institute of Optics University of Rochester, 2000, p. 629.
- [17] N. Sugimoto, "Fabrication and characteristics of bismuth oxide based highly nonlinear fiber," *J. Ceram. Soc. Japan*, vol. 116, no. 1358, pp. 1028–1032, 2008.
- [18] J. Lee and T. Nagashima, "Bismuth-oxide-based nonlinear fiber with a high SBS threshold and its application to four-wave-mixing wavelength conversion using a pure continuous-wave pump," *J. Light.* ..., vol. 24, no. 1, pp. 22–28, 2006.
- [19] M. Dinu, F. Quochi, and H. Garcia, "Third-order nonlinearities in silicon at telecom wavelengths," *Appl. Phys. Lett.*, vol. 82, no. 18, p. 2954, 2003.
- [20] M. Foster, A. Turner, M. Lipson, and A. Gaeta, "Nonlinear optics in photonic nanowires," *Opt. Express*, vol. 16, no. 2, pp. 1070–1078, 2008.
- [21] D. Sarid and W. Challener, *Modern Introduction to Surface Plasmons*, 1st ed. New York: Cambridge University Press, 2010, p. 371.
- [22] R. D. Kekatpure, A. C. Hryciw, E. S. Barnard, and M. L. Brongersma, "Solving dielectric and plasmonic waveguide dispersion relations on a pocket calculator.," *Opt. Express*, vol. 17, no. 26, pp. 24112–29, Dec. 2009.

- [23] E. D. Palik, *Handbook of Optical Constants of Solids*. Boston: Academic Press.
- [24] B. E. A. Saleh and M. C. Teich, *Fundamentals of Photonics*, 1st ed. New York: John Wiley & Sons, Inc., 1991, p. 966.
- [25] M. Rochette, *Module 3: Third-Order Nonlinear Optics*. class notes for ECSE 572, Department of Electrical and Computer Engineering, McGill University at Montreal, Oct. 2011.
- [26] Jianming Jin, *The Finite Element Method in Electromagnetics*, 2nd Ed. New York: John Wiley & Sons, Inc., 2002, p. 753.
- [27] J. Lee, "Finite element analysis of lossy dielectric waveguides," ... *Theory Tech. IEEE Trans.*, vol. 42, no. 6, pp. 1025–1031, 1994.
- [28] L. Petit, N. Carlie, H. Chen, S. Gaylord, J. Massera, G. Boudebs, J. Hu, a. Agarwal, L. Kimerling, and K. Richardson, "Compositional dependence of the nonlinear refractive index of new germanium-based chalcogenide glasses," *J. Solid State Chem.*, vol. 182, no. 10, pp. 2756–2761, Oct. 2009.
- [29] C. Pollock and M. Lipson, *Integrated Photonics*. Springer, 2003.
- [30] A. W. Snyder and J. Love, Optical Waveguide Theory. 1983.
- [31] P. Berini, "Plasmon-polariton waves guided by thin lossy metal films of finite width: Bound modes of asymmetric structures," *Phys. Rev. B*, vol. 63, no. 12, p. 125417, Mar. 2001.
- [32] C. Tsay, E. Mujagić, C. K. Madsen, C. F. Gmachl, and C. B. Arnold, "Mid-infrared characterization of solution-processed As2S3 chalcogenide glass waveguides.," *Opt. Express*, vol. 18, no. 15, pp. 15523–30, Jul. 2010.
- [33] H. Lin, L. Li, Y. Zou, S. Danto, J. D. Musgraves, K. Richardson, S. Kozacik, M. Murakowski, D. Prather, P. T. Lin, V. Singh, A. Agarwal, L. C. Kimerling, and J. Hu, "Demonstration of high-Q mid-infrared chalcogenide glass-on-silicon resonators.," *Opt. Lett.*, vol. 38, no. 9, pp. 1470–2, May 2013.
- [34] S. Jette-Charbonneau, N. Lahoud, R. Charbonneau, G. Mattiussi, and P. Berini, "End-Facet Polishing of Surface Plasmon Waveguides in Lithium Niobate," *IEEE Trans. Adv. Pack.*, vol. 31, no. 3, pp. 479–483, 2008.
- [35] Y. Satuby and M. Orenstein, "Surface-Plasmon-Polariton modes in deep metallic trenches-measurement and analysis," *Opt. Express*, vol. 15, no. 7, pp. 4247–52, Apr. 2007.